Wrinkle generation in shear-enforced rectangular membrane

AUTHOR(S):

Senda, Kei; Petrovic, Mario; Nakanishi, Kei

CITATION:

Senda, Kei ...[et al]. Wrinkle generation in shear-enforced rectangular membrane. Acta Astronautica 2015, 111: 110-135

ISSUE DATE:

2015-06

URL:

http://hdl.handle.net/2433/196845

Wrinkle Generation in Shear-Enforced Rectangular Membrane

Kei Senda[1,*], Mario Petrovic[2], Kei Nakanishi[2]

Kyoto University, Kyoto daigaku-Katsura, Nishikyo-ku, Kyoto 615-8530, Japan

Abstract

The objective of this study is to clarify the wrinkle behavior of a flat rectangular membrane undergoing shear displacement. To achieve this goal, an equilibrium path tracking method using a finite element method is developed. This method includes a bifurcation path tracking analysis that searches for bifurcation solutions. This method establishes an image of the membrane behavior by calculating a series of successive equilibrium states before and after bifurcation buckling. Generally in experiments, flat rectangular membranes have shear displacement imposed on top or bottom edges, while the left and right sides have free boundaries. At large values of shear displacement, the wrinkles cover the entire membrane, but the free boundaries result in uneven shapes and distributions. Further increase in shear results in small wrinkles, referred to as collapsed sections, generated on existing wrinkles. As collapsed sections grow, new wrinkles are generated. However, the universality of this wrinkle generation mechanism may be affected by the free boundaries. By applying cyclic boundary conditions, effects of free boundaries, which include uneven wrinkle shape and distribution, can be eliminated. In addition, by changing the membrane aspect ratio, the effects of geometry are also evaluated. For all membranes, the wrinkle generation from collapsed sections is observed and its independence from free boundaries and aspect ratio is shown. By analyzing stress and displacement fields, the formation of collapsed sections is explained. In addition, for the cyclic boundary conditions, the change in aspect ratio results in almost the same bifurcation structure. Therefore, the wrinkle behavior evaluation in this study can be useful in predicting wrinkle behavior.

Keywords: Membrane wrinkling, Bifurcation structure, FEM

*Corresponding author

Email addresses: senda@kuaero.kyoto-u.ac.jp (Kei Senda), mapetrov@live.com (Mario Petrovic), keinakanishi5@gmail.com (Kei Nakanishi)

[1]Professor, Department of Aeronautics and Astronautics, Graduate School of Engineering, tel: +81-75-383-3761

[2]Graduate Student, Department of Aeronautics and Astronautics, Graduate School of Engineering

1. Introduction

When the structure and design of space vehicles are considered, weight and storage requirements are key limiting factors. Inflatable structures have attracted attention because such structures satisfy the above factors[1]. This study considers structures using deployable membranes. The structures are initially folded, deployed into their desired shape, unfolded or inflated, and rigidized.

The research goal of this study is to achieve stable deployment along a planned trajectory for a structure folded into a prescribed shape. However, because the structure is a membrane, with many degrees of freedom, the prediction of membrane behavior is difficult. Here membrane behavior refers to displacement of membrane points under the effect of external loads. In a deployment experiment using an inflatable tube[2], an origami-like pattern was designed to facilitate predictable deployment. However, small compressive forces cause local buckling and generates wrinkles. Buckling occurs after a bifurcation[3, 4, 5, 6]. When the bifurcation occurs, the material may become unstable and the subsequent state may not be uniquely determined. This makes predicting stable deployment difficult. To solve this problem, understanding of wrinkle behavior is essential.

Buckling results in a finite deformation occurring in a direction different from the direction of the load applied to the structure. In this study, a wrinkle represents this finite deformation. Therefore, a wrinkle is defined as an out-of-plane membrane deformation that occurs when a compressive load is applied to a membrane.

An equilibrium state, or an equilibrium point, is defined as the static state of a membrane when a static load or an imposed displacement is applied. By varying a path parameter such as displacement or load, an equilibrium path is obtained, i.e. successive equilibrium points. Bifurcation is a rapid equilibrium point shift and a qualitative change of the equilibrium state when the path parameter varies. A wrinkle, i.e. buckling of a membrane, is generated after a bifurcation. Therefore, in order to deploy a membrane structure along a planned trajectory, understanding of the bifurcation structure and the equilibrium paths is necessary.

The first step in analyzing wrinkling behavior is modeling the membrane structure. A continuum model based on partial differential equations and a Finite Element (FE) model are typical approaches, however the former yields solutions for only simple systems. Therefore, finite element modeling is used to analyze wrinkle behavior. In previous studies[7, 8, 9], membrane structures were modeled with the membrane elements that ignore bending stiffness. The membrane elements approach excels in terms of computational cost, however it can not accurately calculate the out-of-plane deformation. By using shell elements that include bending stiffness, wrinkle amplitude and wavelength are more accurately calculated.

In a straight column or flat plate, the bifurcation after which buckling occurs is a branching bifurcation[3, 10]. For a flat membrane, it is believed that a wrinkle is generated by bifurcation. Therefore the number of wrinkles increases

after bifurcation. A bifurcation is a singularity in the analysis. Therefore, obtaining equilibrium points after bifurcation is difficult and numerous studies have been conducted[11]. A method for bifurcation path analysis is needed to obtain equilibrium points after bifurcation.

The arc length method, the introduction of imperfections and dynamic analysis, are the common methods for path tracking after bifurcations[12, 6]. However, these methods do not always yield a solution, they change the bifurcation structure, or they obtain a fraction of paths after the bifurcation. To overcome this problem, a bifurcation path analysis method that is able to search for solutions after bifurcation is needed. In this study, a method of searching for bifurcation solutions is added into the equilibrium path tracking method, of Wagner and Wriggers[13].

Membrane wrinkling studies have mostly focused on certain effects on characteristics, i.e. gravity[14], creases[15], stress concentrations[16], etc. In general, wrinkling is analyzed as a membrane behavior event, and wrinkled geometry is computed for specific loads. The goal of this study is to obtain a comprehensive image/understanding of membrane wrinkling. For that purpose, several wrinkle generations, multiple wrinkle configurations, and wrinkle interaction will be considered.

In previous studies[4, 17], a flat rectangular membrane with free boundary conditions was sheared. In Wong and Pellegrino[5, 6], a wide range of numerical results were shown. In addition, Senda, et al. [22] showed the wrinkle behavior for relatively small values of imposed shear. The membrane becomes fully wrinkled for small values of shear. However, it was also shown that the shape and distribution of the wrinkles is not uniform due to the influence of the the free boundaries.

In this study, by increasing the shear displacement in a fully wrinkled membrane, the wrinkle behavior, and the mechanism behind it, is shown. The increase in shear displacement results in small wrinkles generated near the fixed boundaries on existing wrinkles. These small wrinkles will be referred as collapsed sections to distinguish them from the larger, existing wrinkles. By increasing the shear displacement further, the collapsed sections expand along the length of existing wrinkles. At a critical size, the sections perform an unstable expansion, they join in the middle of the existing wrinkle, split it and result in two new wrinkles. This behavior repeats with further increase in shear and represents the basic behavior for wrinkle increase when the membrane is fully wrinkled.

Originally, this behavior is observed for a membrane with an aspect ratio of 3:1 and free boundary conditions. Therefore, it is possible that this membrane behavior is a result of the free boundary effects, and therefore, it may not be universal. To eliminate the effects of free boundaries, in this study the membrane is modeled with cyclic boundaries. Furthermore, to evaluate the effects of geometry, the cyclic boundary membrane is modeled with the aspect ratio of 1:1. For all the membranes, the above described behavior of wrinkle generation by collapsed sections is observed, independently of the boundaries and aspect ratio. Additionally, the behavior of collapsed sections will be explained in detail

through displacement and stress analysis.

The rest of this paper is organized as follows. Section 2 sets up the FEM model of the rectangular membrane using ABAQUS, a FEM software package, the path analysis method and the asymptotic theory to a load parameter. Section 3 shows the path tracking method for a system with an imposed displacement. Section 4 introduces the similarity value and bifurcation diagram. Section 5 presents some numerical simulations and discusses the results. Section 6 offers some concluding remarks.

2. Modeling and problem

2.1. Analyzed object and model

The membrane analyzed in this study is a flat membrane as illustrated in Fig. 1. The material is Kapton and its properties are listed in Table 1. The choice of a Kapton membrane comes from the flat membrane wrinkling data, e.g. Wong and Pellegrino[4] and Inoue[17]. The ratio of the horizontal and the vertical lengths $a : b$ is $3 : 1$. Fixed boundaries are set for the top and bottom edges, and cyclic boundaries for the left and right edges. The fixed top edge is then subjected to prescribed displacement. Gravity and imperfections are not considered.

In this study, 3 different membranes will be used to discuss the results; $a : b = 3 : 1$ with cyclic boundary conditions, $a : b = 3 : 1$ with free boundary conditions, and $a : b = 1 : 1$ with cyclic boundary conditions. The main discussion is based on a membrane with an aspect ratio of $a : b = 3 : 1$ with cyclic boundary conditions, and unless specified otherwise, the discussion refers to this model.

The origin of the xyz-coordinate system is fixed at the membrane center of mass in the undeformed state, i.e. when no external loads are applied. The x-axis is parallel to the bottom edge, y-axis is perpendicular to the bottom edge, and z-axis is normal to the neutral plane, as defined in Fig. 1. Coordinates (x, y, z) refer to a position on the membrane prior to deformation, and they do not vary with deformation. Section AA' is defined at $y = 0$[m] and BB' at $y = -0.045$[m].

First, at the top fixed edge, a displacement of $\delta u_y = 30 \times 10^{-6}$[m] is applied in the y-direction and is constant throughout the analysis. This is to maintain

Table 1: Membrane material properties.

Membrane width	a	0.30 [m]
Membrane height	b	0.10 [m]
Membrane thickness	h	12.5×10^{-6} [m]
Young's Modulus	E	3.0 [GPa]
Poisson's ratio	ν	0.3

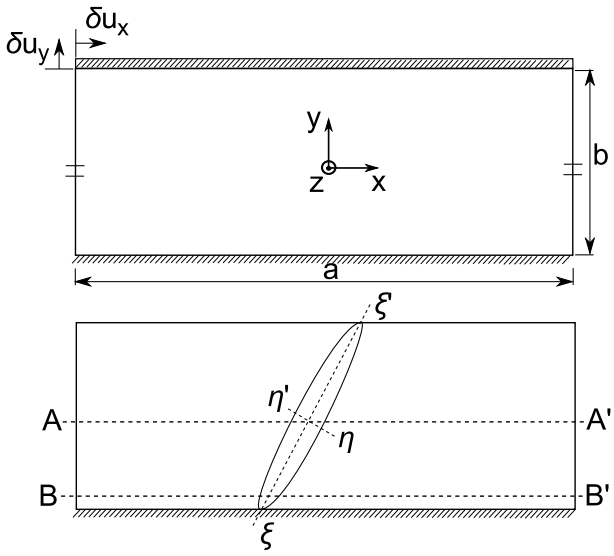

Figure 1: Sheared square membrane. Top and bottom edges have fixed boundaries. Right and left edges have free boundaries.

consistency with experimental results in Inoue[17]. Then, an imposed displacement δu_x in x direction is applied. In this study, δu_x is increased from 0[m] to 510×10^{-6}[m].

Membrane deformation is described by displacements at all points on the membrane. Point displacements are represented by (u_x, u_y, u_z) in (x, y, z) coordinates. However, the z-displacement of points on the mid-plane is mainly considered, where displacement of a point in z-coordinate $u_z(x, y, 0)$ is simply expressed by $u_z(x, y)$.

Stress and strain are given for the mid-plane. The tensile direction is positive for both stress and strain. Considering the plane stress, the $\xi\xi'$-axis corresponds to the first principal stress direction and the $\eta\eta'$-axis corresponds to the second principal stress direction. When wrinkles exist, the $\xi\xi'$-axis in a the wrinkle longitudinal direction is perpendicular to $\eta\eta'$-axis. Both $\xi\xi'$ and $\eta\eta'$ rotate with the wrinkles and remain perpendicular to each other. A wrinkle is defined as a sinusoidal shaped out-of-plane deformation that occurs between two points where curvature in η-direction changes sign.

The problems dealt with in this study are defined below. The membrane behavior is analyzed by increasing the imposed shear displacement δu_x. The behavior includes wrinkle geometry indicated by the displacement $u_z(x, y)$, bifurcation structure of the deformation, and stress. Stress values as well as forces and moments at certain points will be used to explain the behavior in more detail. The wrinkle generation mechanism is described by the following analysis.

2.2. Differential equations

The first step in the analysis of membrane wrinkling is establishing the governing equations for plates[3]. These equations provide the key properties of the system. For membranes, the Kirchhoff-Love assumptions for thin plates are adopted. By taking the standard plate definitions[3] the plate equations are written as:

$$\begin{aligned}
&\frac{Eh}{1-\nu^2}\left[\frac{\partial^2 u_x}{\partial x^2}+\frac{\partial u_z}{\partial x}\left(\frac{\partial^2 u_z}{\partial x^2}\right)+\nu\left\{\frac{\partial^2 u_y}{\partial x\partial y}+\frac{\partial u_z}{\partial y}\frac{\partial^2 u_z}{\partial x\partial y}\right\}\right]\\
&+\frac{Eh}{2(1+\nu)}\left\{\frac{\partial^2 u_x}{\partial y^2}+\frac{\partial^2 u_y}{\partial x\partial y}+\frac{\partial^2 u_z}{\partial x\partial y}\frac{\partial u_z}{\partial y}+\frac{\partial u_z}{\partial x}\frac{\partial^2 u_z}{\partial y^2}\right\}\\
&=f_x(u_x,\,u_y,\,u_z)=0 \qquad (1)\\
&\frac{Eh}{1-\nu^2}\left[\frac{\partial^2 u_x}{\partial y^2}+\frac{\partial u_z}{\partial y}\left(\frac{\partial^2 u_z}{\partial y^2}\right)+\nu\left\{\frac{\partial^2 u_x}{\partial x\partial y}+\frac{\partial u_z}{\partial x}\frac{\partial^2 u_z}{\partial x\partial y}\right\}\right]\\
&+\frac{Eh}{2(1+\nu)}\left\{\frac{\partial^2 u_y}{\partial x^2}+\frac{\partial^2 u_x}{\partial x\partial y}+\frac{\partial^2 u_z}{\partial x\partial y}\frac{\partial u_z}{\partial x}+\frac{\partial u_z}{\partial y}\frac{\partial^2 u_z}{\partial x^2}\right\}\\
&=f_y(u_x,\,u_y,\,u_z)=0 \qquad (2)\\
&-D\left(\frac{\partial^4 u_z}{\partial x^4}+\nu\frac{\partial^4 u_z}{\partial x^2\partial y^2}\right)-2D(1-\nu)\frac{\partial^4 u_z}{\partial x^2\partial y^2}-D\left(\frac{\partial^4 u_z}{\partial y^4}+\nu\frac{\partial^4 u_z}{\partial x^2\partial y^2}\right)\\
&+\frac{Eh}{1-\nu^2}\left\{\frac{\partial^2 u_x}{\partial x^2}+\frac{\partial^2 u_z}{\partial x^2}+\nu\left(\frac{\partial^2 u_x}{\partial x\partial y}+\frac{\partial u_z}{\partial y}\frac{\partial^2 u_z}{\partial x\partial y}\right)\right\}\frac{\partial u_z}{\partial x}\\
&+\frac{Eh}{2(1+\nu)}\left(\frac{\partial^2 u_x}{\partial x\partial y}+\frac{\partial^2 u_y}{\partial x^2}+\frac{\partial^2 u_z}{\partial x^2}\frac{\partial u_z}{\partial y}+\frac{\partial u_z}{\partial x}\frac{\partial^2 u_z}{\partial x\partial y}\right)\frac{\partial u_z}{\partial y}\\
&+\frac{Eh}{1-\nu^2}\left\{\frac{\partial^2 u_x}{\partial y^2}+\frac{\partial u_z}{\partial y}\frac{\partial^2 u_z}{\partial y^2}+\nu\left(\frac{\partial^2 u_x}{\partial x\partial y}+\frac{\partial^2 u_z}{\partial x\partial y}\right)\right\}\frac{\partial u_z}{\partial y}\\
&+\frac{Eh}{2(1+\nu)}\left(\frac{\partial^2 u_x}{\partial y^2}+\frac{\partial^2 u_y}{\partial x\partial y}+\frac{\partial^2 u_z}{\partial x\partial y}\frac{\partial u_z}{\partial y}+\frac{\partial u_z}{\partial x}\frac{\partial^2 u_z}{\partial y^2}\right)\frac{\partial u_z}{\partial x}\\
&=f_z(u_x,\,u_y,\,u_z)=0 \qquad (3)
\end{aligned}$$

where D is membrane bending stiffness. The above equations are grouped as:

$$\boldsymbol{f}(\boldsymbol{u}(\boldsymbol{x}))=\begin{bmatrix} f_x(u_x(x,\,y,\,z),\,u_y(x,\,y,\,z),\,u_z(x,\,y,\,z))\\ f_y(u_x(x,\,y,\,z),\,u_y(x,\,y,\,z),\,u_z(x,\,y,\,z))\\ f_z(u_x(x,\,y,\,z),\,u_y(x,\,y,\,z),\,u_z(x,\,y,\,z))\end{bmatrix}=\mathbf{0} \qquad (4)$$

The boundary conditions are given by:

$$u_x(x, -\frac{b}{2}, 0) = 0 \quad u_y(x, -\frac{b}{2}, 0) = 0$$
$$u_z(x, -\frac{b}{2}, 0) = 0 \quad (-\frac{a}{2} \leq x \leq \frac{a}{2}) \tag{5}$$
$$u_x(x, \frac{b}{2}, 0) = \delta u_x \quad u_y(x, \frac{b}{2}, 0) = \delta u_y$$
$$u_z(x, \frac{b}{2}, 0) = 0 \quad (-\frac{a}{2} \leq x \leq \frac{a}{2}) \tag{6}$$
$$u_x(-\frac{a}{2}, y, 0) = u_x(\frac{a}{2}, y, 0) \quad u_y(-\frac{a}{2}, y, 0) = u_y(\frac{a}{2}, y, 0)$$
$$u_z(-\frac{a}{2}, y, 0) = u_z(-\frac{a}{2}, y, 0) \quad (-\frac{1}{2}b \leq y \leq \frac{1}{2}b) \tag{7}$$
$$\frac{\partial u}{\partial x}(-\frac{a}{2}, y, 0) = \frac{\partial u}{\partial x}(\frac{a}{2}, y, 0) \quad \frac{\partial u}{\partial y}(-\frac{a}{2}, y, 0) = \frac{\partial u}{\partial y}(\frac{a}{2}, y, 0)$$
$$\frac{\partial u}{\partial z}(-\frac{a}{2}, y, 0) = \frac{\partial u}{\partial z}(\frac{a}{2}, y, 0) \quad (-\frac{1}{2}b \leq y \leq \frac{1}{2}b) \tag{8}$$
$$\frac{\partial u_z}{\partial x}(x, \pm\frac{b}{2}, 0) = 0 \quad \frac{\partial u_z}{\partial y}(x, \pm\frac{b}{2}, 0) = 0$$
$$\frac{\partial u_z}{\partial z}(x, \pm\frac{b}{2}, 0) = 0 \quad (-\frac{a}{2} \leq x \leq \frac{a}{2}) \tag{9}$$

Equations (7) and (8) represent a part of cyclic boundary conditions that are necessary for this system. While it is not possible to analytically solve these equations, they can be used to determine system symmetry to explain membrane behavior. This topic is discussed in a later section.

2.3. Finite element method (FEM) model

The above geometry, properties and boundary conditions are modeled using ABAQUS, a finite element method software. We use the S4R shell elements provided by ABAQUS. For the mesh, equivalent divisions in x and y directions are constructed, resulting in an element number of 360×120. The validity of this element number is discussed in Section 5. It should be noted that only geometric nonlinearity is considered. Nonlinearity due to other factors such as material are not considered in the present study.

The static equilibrium of forces, i.e. nonlinear FEM based equations on the displacement method, are formally written as:

$$\boldsymbol{F}(\boldsymbol{u}, \boldsymbol{f}) = \boldsymbol{0} \tag{10}$$

where $\boldsymbol{f}$ is the applied force for displacement $\boldsymbol{u}$. The static problem solves the equilibrium equation with δu_x for the equilibrium point $(\boldsymbol{u}, \boldsymbol{f})$. The imposed displacement δu_x is included in $\boldsymbol{u}$ and the constraint forces for displacement $\boldsymbol{u}$ are included in $\boldsymbol{f}$. Eq. (10) is a nonlinear equation of $\boldsymbol{u}$ and $\boldsymbol{f}$, which is difficult

to solve. The solution method, e.g. an incremental calculation, is explained in the next section.

3. Equilibrium path tracking method

For equilibrium path tracking, a new equilibrium point, near the current equilibrium point, is determined by slightly changing the path parameter. However, if the new point is a bifurcation point, a bifurcation path analysis method is needed to search for post-bifurcation points because a bifurcation point is a singularity in the analysis. A bifurcation diagram shows the relative position of equilibrium points before and after the bifurcation point. The bifurcation diagram and deformation must be obtained in order to understand membrane behavior at the bifurcation points within path parameters.

First, from an analytical standpoint, the possible bifurcation structures will be discussed based on the asymptotic theory discussed in Endo[18] where the path parameter is load. Because the path parameter in this study is displacement, the relation between load and displacement is established. The relationship between the deformed state of the membrane $\boldsymbol{u}$ and the incremental displacement δu_x will be established, where the displacement δu_x is the path parameter. Finally, a method for searching for bifurcation solutions equivalent to that of Wagner and Wriggers[13] is built into the equilibrium path tracking method. This search consists of a stability inspection of the tangent stiffness matrix. Near bifurcation points the relevant eigenvectors are used to obtain bifurcation solutions. The process will be discussed in more detail later on.

Because this study does not consider imperfections, the following discussion about bifurcation points will be based on perfect bifurcations. If imperfections are considered, the bifurcation structure changes. A bifurcation point is removed and the equilibrium path that was leading to the bifurcation point now connects directly into one of the post-bifurcation paths. Instead of branching paths after a bifurcation, the imperfections select one path. Gravity has a similar effect; it acts as a disturbance that selects a single path at a bifurcation. By considering these effects, the bifurcation is reduced to a single continuous equilibrium path.

3.1. Successive solution calculation

For successive solutions to nonlinear equations, the relationship between increments in load, $\boldsymbol{f}$, and displacement, $\boldsymbol{u}$, is shown. The relationship to incremental imposed displacement, δu_x, will be discussed later.

An equilibrium point $(\boldsymbol{u}_0 + \tilde{\boldsymbol{u}},\ \boldsymbol{f}_0 + \tilde{\boldsymbol{f}})$ close to a given equilibrium point $(\boldsymbol{u}_0,\ \boldsymbol{f}_0)$ of Eq. (10) satisfies

$$\boldsymbol{F}(\boldsymbol{u}_0 + \tilde{\boldsymbol{u}},\ \boldsymbol{f}_0 + \tilde{\boldsymbol{f}}) = \boldsymbol{0} \tag{11}$$

Expanding Eq. (11) in a Taylor series and by omitting the higher order terms gives

$$\boldsymbol{K}\tilde{\boldsymbol{u}} = \tilde{\boldsymbol{f}} \tag{12}$$

where $\boldsymbol{K} = \dfrac{\partial \boldsymbol{F}}{\partial \boldsymbol{u}^T}$ is the tangent stiffness matrix.

A solution at the new equilibrium point, $(\boldsymbol{u}_0+\tilde{\boldsymbol{u}},\ \boldsymbol{f}_0+\tilde{\boldsymbol{f}})$, of the original nonlinear equation (11) is determined by iterative methods, e.g. Newton-Raphson method. This is the equilibrium path tracking method to seek successive equilibrium points by gradually increasing $\boldsymbol{f}$ (or δu_x). Also, it is the static solution method that obtains solutions satisfying the static equilibrium equation (10). However, the structure bifurcation point $(\boldsymbol{u}_c, \boldsymbol{f}_c)$ is singular, i.e. $\det \boldsymbol{K} = 0$. The incremental displacement $\tilde{\boldsymbol{u}}$ corresponding to incremental load $\tilde{\boldsymbol{f}}$ cannot be uniquely determined.

3.2. Asymptotic theory of bifurcation analysis

In order to correctly track paths after a bifurcation, a prediction of the bifurcation structure and post-bifurcation behavior is desired. Some bifurcation analyses based on asymptotic theory have been presented[18]. Although they are for static loads, they are helpful. Because experiments usually use imposed displacements, an asymptotic theory of bifurcation analysis for imposed displacement is needed. The following is an overview of bifurcation analysis for a static load.

3.2.1. Nonlinear equation solution

An equilibrium of a system is represented by Eq. (10). An equilibrium point $(\boldsymbol{u}_*,\ f_*)$ is calculated close to the given equilibrium point $(\boldsymbol{u}^{(i)},\ f_i)$. By setting $(\boldsymbol{u}_*,\ f_*) = (\boldsymbol{u}^{(i)} + \tilde{\boldsymbol{u}}^{(i+1)},\ f_*)$, the following equation for $i = 0, 1, 2, 3, \ldots$ is obtained.

$$\begin{aligned}\boldsymbol{F}(\boldsymbol{u}^{(i)} + \tilde{\boldsymbol{u}}^{(i+1)},\ f_*) = \boldsymbol{F}(\boldsymbol{u}^{(i)},\ f_*) + \frac{\partial \boldsymbol{F}}{\partial \boldsymbol{u}^T}(\boldsymbol{u}^{(i)})\tilde{\boldsymbol{u}}^{(i+1)} \\ + \frac{1}{2!}\tilde{\boldsymbol{u}}^{(i+1)\ T}\frac{\partial^2 \boldsymbol{F}}{\partial \boldsymbol{u}\partial \boldsymbol{u}^T}(\boldsymbol{u}^{(i)})\tilde{\boldsymbol{u}}^{(i+1)} + \cdots = \boldsymbol{0}\end{aligned} \tag{13}$$

where higher order terms are omitted. Rearranging gives:

$$\tilde{\boldsymbol{u}}^{(i+1)} \approx -\boldsymbol{K}_i^{-1}\boldsymbol{F}(\boldsymbol{u}^{(i)},\ f_*) \tag{14}$$

where $\boldsymbol{K}_i = \dfrac{\partial \boldsymbol{F}}{\partial \boldsymbol{u}^T}(\boldsymbol{u}^{(i)})$ is the tangent stiffness matrix at $\boldsymbol{u}^{(i)}$.

Calculation of $\boldsymbol{F}(\boldsymbol{u}^{(1)},\ f_*)$, $\boldsymbol{F}(\boldsymbol{u}^{(2)}, f_*)$, $\ldots$, $\boldsymbol{F}(\boldsymbol{u}^{(n)},\ f_*)$ is performed until $\boldsymbol{F}(\boldsymbol{u}^{(n)},\ f_*) = \boldsymbol{0}$.

3.2.2. Asymptotic theory near the bifurcation point

When determinants of the tangent stiffness matrices $\boldsymbol{K}_0, \boldsymbol{K}_1, \boldsymbol{K}_2, \ldots$ are zero, the increments toward the next equilibrium point, $\tilde{\boldsymbol{u}}^{(1)},\ \tilde{\boldsymbol{u}}^{(2)},\ \tilde{\boldsymbol{u}}^{(3)}, \ldots$ cannot be determined uniquely. At a bifurcation point, the tangent stiffness matrix has at least one zero eigenvalue. Solution $(\boldsymbol{u}^{(i)},\ f_i)$ is called a simple singular point when tangent stiffness matrix $\boldsymbol{K}_i$ has one zero eigenvalue. Following Endo, et al[18], a bifurcation point $(\boldsymbol{u}_c,\ f_c)$ that is a simple singular

point is discussed. At a bifurcation point $(\boldsymbol{u}_c,\, f_c)$, the expanded incremental equation based on Eq. (10) becomes:

$$\boldsymbol{F}(\boldsymbol{u}_c,\, f_c) + \boldsymbol{K}_c\tilde{\boldsymbol{u}} + \left(\frac{\partial \boldsymbol{F}}{\partial f}\right)_c \tilde{f} + \cdots - \boldsymbol{F}(\boldsymbol{u}_c,\, f_c) = \boldsymbol{0} \tag{15}$$

where infinitesimally small increments of displacement $\tilde{\boldsymbol{u}}$ and load $\tilde{f}$, are considered. The eigenvalues and the corresponding eigenvectors of $\boldsymbol{K}_c$, respectively, are $\lambda_1,\, \lambda_2,\, \ldots,\, \lambda_n$ and $\boldsymbol{\phi}_1,\, \boldsymbol{\phi}_2,\, \ldots,\, \boldsymbol{\phi}_n$ which are normalized. All eigenvalues are real and $\lambda_1 = 0$. The basis matrix $\boldsymbol{\Phi}$ is the column matrix of eigenvectors. The incremental displacement vector $\tilde{\boldsymbol{u}}$ is approximated using the system eigenvectors as:

$$\tilde{\boldsymbol{u}} = \boldsymbol{\Phi}\tilde{\boldsymbol{q}} = \begin{bmatrix} \boldsymbol{\phi}_1 & \boldsymbol{\phi}_2 & \cdots & \boldsymbol{\phi}_n \end{bmatrix} \begin{bmatrix} \tilde{q}_1 \\ \tilde{q}_2 \\ \vdots \\ \tilde{q}_n \end{bmatrix} \tag{16}$$

Using the basis matrix $\boldsymbol{\Phi}$, the tangent stiffness matrix is expressed using eigenvector diagonalization as:

$$\boldsymbol{K}_c = \frac{\partial \boldsymbol{F}}{\partial \boldsymbol{u}^T}(\boldsymbol{u}_c,\, f_c) = \left(\frac{\partial \boldsymbol{F}}{\partial \boldsymbol{u}^T}\right)_c = \boldsymbol{\Phi} \begin{bmatrix} \lambda_1 & 0 & \cdots & 0 \\ 0 & \lambda_2 & \cdots & 0 \\ \vdots & \vdots & \ddots & \vdots \\ 0 & 0 & \cdots & \lambda_n \end{bmatrix} \boldsymbol{\Phi}^T \tag{17}$$

The coordinate transformation of Eq. (15) yields

$$^{\Phi}\boldsymbol{K}_c\tilde{\boldsymbol{q}} + \boldsymbol{\Phi}^T \left(\frac{\partial \boldsymbol{F}}{\partial f}\right)_c \tilde{f} + \cdots = \boldsymbol{0} \tag{18}$$

$$\begin{bmatrix} \lambda_1\tilde{q}_1 + \boldsymbol{\phi}_1^T \left(\frac{\partial \boldsymbol{F}}{\partial f}\right)_c \tilde{f} + \cdots \\ \lambda_2\tilde{q}_2 + \boldsymbol{\phi}_2^T \left(\frac{\partial \boldsymbol{F}}{\partial f}\right)_c \tilde{f} + \cdots \\ \vdots \\ \lambda_n\tilde{q}_n + \boldsymbol{\phi}_n^T \left(\frac{\partial \boldsymbol{F}}{\partial f}\right)_c \tilde{f} + \cdots \end{bmatrix} = \begin{bmatrix} \tilde{F}_1(\tilde{\boldsymbol{q}}, \tilde{f}) \\ \tilde{F}_2(\tilde{\boldsymbol{q}}, \tilde{f}) \\ \vdots \\ \tilde{F}_n(\tilde{\boldsymbol{q}}, \tilde{f}) \end{bmatrix} = \boldsymbol{0} \tag{19}$$

where $^{\Phi}\boldsymbol{K}_c$ is the rotated tangent stiffness matrix. Solution for increments

relating to specific eigenvectors is:

$$\tilde{q_2} = -\frac{1}{\lambda_2}\left(\boldsymbol{\phi}_2^T \left(\frac{\partial \boldsymbol{F}}{\partial f}\right)_c \tilde{f} + \cdots\right) \tag{20}$$

$$\vdots$$

$$\tilde{q}_n = -\frac{1}{\lambda_n}\left(\boldsymbol{\phi}_n^T \left(\frac{\partial \boldsymbol{F}}{\partial f}\right)_c \tilde{f} + \cdots\right) \tag{21}$$

By substituting $\tilde{q}_2$, $\tilde{q}_3$, …, $\tilde{q}_n$ functions of $\tilde{q}_1$ and $\tilde{f}$ into Eq. (19), the equation for the singular state of the system can be expressed as:

$$\tilde{F_1}(\tilde{\boldsymbol{q}}, \tilde{f}) = \tilde{F_1}(\tilde{q}_1, \tilde{f}) = 0 \tag{22}$$

Equation (22) is expanded into a Taylor series, which yields

$$\tilde{F_1}(0,\,0) + \sum_{i=1}^{n} \frac{1}{i!}\frac{\partial^i \tilde{F_1}}{\partial \tilde{q}_1^i}\tilde{q}_1^i + \sum_{i=1}^{n} \frac{1}{i!}\frac{\partial^i \tilde{F_1}}{\partial \tilde{f}^i}\tilde{f}^i + \sum_{i=1}^{n}\sum_{j=1}^{n} \frac{1}{(i+j)!}\frac{\partial^{i+j} \tilde{F_1}}{\partial \tilde{q}_1^i \partial \tilde{f}^j}\tilde{q}_1^i \tilde{f}^j = 0 \tag{23}$$

$$A_{00} + (A_{10}\tilde{q}_1 + \cdots) + (A_{01}\tilde{f} + \cdots) + (A_{11}\tilde{q}_1\tilde{f} + \cdots) = 0 \tag{24}$$

$$A_{ij} = \frac{1}{i!j!}\frac{\partial^{i+j}}{\partial \tilde{q_1}^i \partial \tilde{f}^j}\tilde{F_1}(0,\,0) \tag{25}$$

The above equation describes the singular state of the system, for a single zero eigenvalue. The type of the bifurcation point will depend on the form of the equation. Depending on the system being analyzed, coefficients A_{ij} will vary and therefore, the types of bifurcation points that occur.

While the discussion in this section focuses on bifurcation points with a single zero eigenvalue, these point are not the only type of bifurcation points. Bifurcation points with multiple zero eigenvalues are also possible.

3.2.3. Classification of bifurcation points

The classification of bifurcation points will be based on several general assumptions. These hold true for all types of bifurcation points. At the bifurcation point, the increments of displacement and load are very small. The system has a single zero eigenvalue, while the remaining eigenvalues are positive. The general form of the singular state as Eq. (24) is considered initially and is reduced

depending on the point considered. These assumptions are expressed as:

$$|\tilde{q}_1| = O(\delta),\ |\tilde{f}| = O(\epsilon),\ 0 < \epsilon \ll 1,\ 0 < \delta \ll 1 \tag{26}$$

$$\lambda_1 = 0,\ \lambda_2 = \cdots = \lambda_n = O(1) \tag{27}$$

$$A_{ij} = O(1) \tag{28}$$

$$\boldsymbol{\phi}_i^T \left(\frac{\partial \boldsymbol{F}}{\partial f} \right)_c = O(1) \quad (i = 2,\ 3,\ \ldots,\ n) \tag{29}$$

According to the asymptotic theory, there exist the following bifurcation points: (i)-a limit point, i.e. maximum or minimum point, (i)-b limit point, i.e. inflection point, (ii)-a asymmetric bifurcation point, and (ii)-b symmetric bifurcation point. The relation between the incremental displacement and the loading parameter is analyzed in each case.

(i)-a Snap-through bifurcation point (maximum and minimum point)

For this type of point, Eq. (24) has the following form:

$$A_{20}\tilde{q}_1^2 + A_{01}\tilde{f} = 0 \tag{30}$$

where $\epsilon \sim \delta^2 \ll \delta$. Therefore, $\tilde{q}_1 \gg \tilde{f}$ and Eqs. (20) to (21) become:

$$\tilde{q}_2 \approx -\frac{1}{\lambda_2}\boldsymbol{\phi}_2^T \left(\frac{\partial \boldsymbol{F}}{\partial f} \right)_c \tilde{f} = O(\tilde{f}) \ll O(\tilde{q}_1) \tag{31}$$

$$\vdots$$

$$\tilde{q}_n \approx -\frac{1}{\lambda_n}\boldsymbol{\phi}_n^T \left(\frac{\partial \boldsymbol{F}}{\partial f} \right)_c \tilde{f} = O(\tilde{f}) \ll O(\tilde{q}_1) \tag{32}$$

where higher order terms are omitted based on Eq. (26). Then Eq. (16) shows the direction of the bifurcation path as:

$$\tilde{\boldsymbol{u}} \approx \tilde{q}_1 \boldsymbol{\phi}_1 \tag{33}$$

The $\tilde{f}$ is a quadratic function of $\tilde{q}_1$, and the bifurcation point is the extremal value of the function. So, $\tilde{q}_1$ changes rapidly for a slight change of $\tilde{f}$.

(i)-b Snap-through bifurcation point (inflection point) ($A_{20} = 0$)

For this type of point, Eq. (24) has the following form:

$$A_{30}\tilde{q}_1^3 + A_{01}\tilde{f} = 0 \tag{34}$$

where $\epsilon \sim \delta^3 \ll \delta$. Therefore, $\tilde{q}_1 \gg \tilde{f}$ meaning $O(\tilde{f}) \ll O(\tilde{q}_1)$. Again, $\tilde{\boldsymbol{u}} \approx \tilde{q}_1 \boldsymbol{\phi}_1$ is the direction of the bifurcation path. The $\tilde{f}$ is a cubic function of $\tilde{q}_1$, and the bifurcation point is the inflection point of the function. So, $\tilde{q}_1$ changes rapidly after a slight change of $\tilde{f}$.

(ii)-a Asymmetric bifurcation point ($A_{01} = 0$, $A_{20}A_{02} - \frac{1}{4}A_{11} < 0$)

For this type of point, Eq. (24) has the following form:

$$A_{20}\tilde{q}_1^2 + A_{11}\tilde{q}_1\tilde{f} = 0 \tag{35}$$

where $\epsilon^2 \ll \delta\epsilon \sim \delta^2 \ll \epsilon \ll \delta$. Again, $\tilde{\boldsymbol{u}} \approx \tilde{q}_1\boldsymbol{\phi}_1$ is the direction of the bifurcation path. $\tilde{q}_1 = 0$ or $\tilde{q}_1$ is a linear function of $\tilde{f}$. $\tilde{q}_1 = 0$ is the primary path. The linear function $A_{20}\tilde{q}_1 + A_{11}\tilde{f} = 0$ is the bifurcation path. At the bifurcation path, $\tilde{q}_1$ is the same order of $\tilde{f}$.

(ii)-b Symmetric bifurcation point ($A_{01} = A_{20} = 0$, $A_{20}A_{02} - \frac{1}{4}A_{11} < 0$)

For this type of point, Eq. (24) has the following form:

$$A_{30}\tilde{q}_1^3 + A_{11}\tilde{q}_1\tilde{f} = 0 \tag{36}$$

where $\epsilon^2 \ll \delta^3 \sim \delta\epsilon \ll \epsilon \ll \delta$. Therefore, $\tilde{q}_1 \gg \tilde{f}$ meaning $O(\tilde{f}) \ll O(\tilde{q}_1)$. Again, $\tilde{\boldsymbol{u}} \approx \tilde{q}_1\boldsymbol{\phi}_1$ is the direction of the bifurcation path. This results in $\tilde{q}_1 = 0$ or $\tilde{q}_1$ is quadratic function of $\tilde{f}$. $\tilde{q}_1 = 0$ is the primary path and a quadratic function $A_{30}\tilde{q}_1^2 + A_{11}\tilde{f} = 0$ is the bifurcation path. So, $\tilde{q}_1$ changes rapidly for a slight change of $\tilde{f}$.

3.3. Imposed displacement and imposed load relation

In this subsection, the analysis method based on nonlinear equations for imposed displacement will be explained in terms of asymptotic theory.

The governing nonlinear equations is Eq. (10). The displacement vector $\boldsymbol{u}$, and the external force vector $\boldsymbol{f}$ are defined as:

$$\boldsymbol{u} = \begin{bmatrix} \underline{\boldsymbol{u}}_1 \\ \underline{\boldsymbol{u}}_{2f} \\ \boldsymbol{u}_{2nof} \end{bmatrix}, \quad \boldsymbol{f} = \begin{bmatrix} \boldsymbol{f}_1 \\ \boldsymbol{f}_{2f} \\ \underline{\boldsymbol{f}}_{2nof} \end{bmatrix} \tag{37}$$

where the underlined variables are known, and those with suffixes 1 and 2 correspond to geometric boundary conditions and loads as mechanical boundary conditions, respectively. In addition, $\underline{\boldsymbol{u}}_1$ represents the degrees of freedom at the top boundary except the degrees of freedom in x-direction and all degrees of freedom at the bottom boundary, therefore $\underline{\boldsymbol{u}}_1 = \boldsymbol{0}$.

The $\underline{\boldsymbol{u}}_{2f}$ are the degrees of freedom on the top boundary in x-direction. The $\boldsymbol{u}_{2nof}$ represents the degrees of freedom of all nodes except at the top and bottom boundaries. Force $\boldsymbol{f}_1$ is the reactive force corresponding to the imposed displacement $\underline{\boldsymbol{u}}_1 = \boldsymbol{0}$. Force $\boldsymbol{f}_{2f}$ is the reactive force corresponding to the imposed displacement $\underline{\boldsymbol{u}}_{2f}$. The $\underline{\boldsymbol{u}}_{2f}$ is a M size vector and $\boldsymbol{u}_{2nof}$ is a N size vector.

The $\underline{\boldsymbol{f}}_{2nof}$ is the external force on the degrees of freedom in $\boldsymbol{u}_{2nof}$, however there is no external force on them, hence $\underline{\boldsymbol{f}}_{2nof} = \boldsymbol{0}$. The original nonlinear

equation becomes:

$$\boldsymbol{F}(\underline{\boldsymbol{u}}_1,\, \underline{\boldsymbol{u}}_{2f},\, \boldsymbol{u}_{2nof},\, \boldsymbol{f}_1,\, \boldsymbol{f}_{2f},\, \underline{\boldsymbol{f}}_{2nof}) = \boldsymbol{0} \tag{38}$$

This equation can be divided into three parts, i.e. the fixed boundary, the boundary with the imposed displacement and the rest of the membrane. Then the nonlinear equations are as:

$$\boldsymbol{F}_1(\underline{\boldsymbol{u}}_1,\, \underline{\boldsymbol{u}}_{2f},\, \boldsymbol{u}_{2nof},\, \boldsymbol{f}_1) = \boldsymbol{0} \tag{39}$$

$$\boldsymbol{F}_{2f}(\underline{\boldsymbol{u}}_1,\, \underline{\boldsymbol{u}}_{2f},\, \boldsymbol{u}_{2nof},\, \boldsymbol{f}_{2f}) = \boldsymbol{0} \tag{40}$$

$$\boldsymbol{F}_{2nof}(\underline{\boldsymbol{u}}_1,\, \underline{\boldsymbol{u}}_{2f},\, \boldsymbol{u}_{2nof},\, \underline{\boldsymbol{f}}_{2nof}) = \boldsymbol{0} \tag{41}$$

A coordinate transformation is performed to reduce the number of variables. By considering the generalized coordinates in x-direction at the top edge, the transformation is:

$$\underline{\boldsymbol{u}}_{2f} = \begin{bmatrix} 1 & 0 & \cdots & 0 & 1 \\ 0 & 1 & \cdots & 0 & 1 \\ \vdots & \vdots & \ddots & \vdots & \vdots \\ 0 & 0 & \cdots & 1 & 1 \\ 0 & 0 & \cdots & 0 & 1 \end{bmatrix} \begin{bmatrix} \underline{u}_{2f1} - \underline{u}_{2fM} \\ \underline{u}_{2f2} - \underline{u}_{2fM} \\ \vdots \\ \underline{u}_{2fM-1} - \underline{u}_{2fM} \\ \underline{u}_{2fM} \end{bmatrix} = \boldsymbol{T}\underline{\boldsymbol{u}}'_{2f}$$

As shown in the equation, the new coordinates are described by the original coordinates $\boldsymbol{u}_{2f}$ and the equation can be solved for $\underline{\boldsymbol{u}}'_{2f}$ in reverse, thus $\underline{\boldsymbol{u}}'_{2f}$ is also a generalized coordinate. Substituting this relation into the above equations, considering the constraint condition $\underline{\boldsymbol{u}}_{2f} = \delta\underline{u}_x\underline{\boldsymbol{e}}$, and the vector $\underline{\boldsymbol{c}}$ as the constant vector:

$$\underline{\boldsymbol{c}} = [0 \quad \cdots \quad 0 \quad 1]^T \tag{42}$$

the Taylor expansion by using the relationships $\underline{\boldsymbol{u}}_{2f} = \boldsymbol{T}\underline{\boldsymbol{u}}'_{2f} = \boldsymbol{T}\underline{\boldsymbol{c}}\delta\underline{u}_x$ is performed:

$$\frac{\partial \boldsymbol{F}_1}{\partial \underline{\boldsymbol{u}}_1^T}\tilde{\underline{\boldsymbol{u}}}_1 + \frac{\partial \boldsymbol{F}_1}{\partial \boldsymbol{u}_{2f}^T}\boldsymbol{T}\underline{\boldsymbol{c}}\delta\tilde{\underline{u}}_x + \frac{\partial \boldsymbol{F}_1}{\partial \boldsymbol{u}_{2nof}^T}\tilde{\boldsymbol{u}}_{2nof} + \frac{\partial \boldsymbol{F}_1}{\partial \boldsymbol{f}_1^T}\tilde{\boldsymbol{f}}_1 + \cdots = \boldsymbol{0} \tag{43}$$

$$\frac{\partial \boldsymbol{F}_{2f}}{\partial \underline{\boldsymbol{u}}_1^T}\tilde{\underline{\boldsymbol{u}}}_1 + \frac{\partial \boldsymbol{F}_{2f}}{\partial \boldsymbol{u}_{2f}^T}\boldsymbol{T}\underline{\boldsymbol{c}}\delta\tilde{\underline{u}}_x + \frac{\partial \boldsymbol{F}_{2f}}{\partial \boldsymbol{u}_{2nof}^T}\tilde{\boldsymbol{u}}_{2nof} + \frac{\partial \boldsymbol{F}_{2f}}{\partial \boldsymbol{f}_{2f}^T}\tilde{\boldsymbol{f}}_{2f} + \cdots = \boldsymbol{0} \tag{44}$$

$$\frac{\partial \boldsymbol{F}_{2nof}}{\partial \underline{\boldsymbol{u}}_1^T}\tilde{\underline{\boldsymbol{u}}}_1 + \frac{\partial \boldsymbol{F}_{2nof}}{\partial \boldsymbol{u}_{2f}^T}\boldsymbol{T}\underline{\boldsymbol{c}}\delta\tilde{\underline{u}}_x + \frac{\partial \boldsymbol{F}_{2nof}}{\partial \boldsymbol{u}_{2nof}^T}\tilde{\boldsymbol{u}}_{2nof} + \frac{\partial \boldsymbol{F}_{2nof}}{\partial \underline{\boldsymbol{f}}_{2nof}^T}\tilde{\underline{\boldsymbol{f}}}_{2nof} + \cdots = \boldsymbol{0} \tag{45}$$

where the $\tilde{\boldsymbol{u}}$ and $\tilde{\boldsymbol{f}}$ are increments in displacements and loads. The linear parts

of the above equations are rewritten in matrix forms as:

$$\begin{bmatrix} \frac{\partial \boldsymbol{F}_1}{\partial \underline{\boldsymbol{u}}_1^T} & \frac{\partial \boldsymbol{F}_1}{\partial \boldsymbol{u}_{2f}^T}\boldsymbol{T} & \frac{\partial \boldsymbol{F}_1}{\partial \boldsymbol{u}_{2nof}^T} \\ \frac{\partial \boldsymbol{F}_{2f}}{\partial \underline{\boldsymbol{u}}_1^T} & \frac{\partial \boldsymbol{F}_{2f}}{\partial \boldsymbol{u}_{2f}^T}\boldsymbol{T} & \frac{\partial \boldsymbol{F}_{2f}}{\partial \boldsymbol{u}_{2nof}^T} \\ \frac{\partial \boldsymbol{F}_{2nof}}{\partial \underline{\boldsymbol{u}}_1^T} & \frac{\partial \boldsymbol{F}_{2nof}}{\partial \boldsymbol{u}_{2f}^T}\boldsymbol{T} & \frac{\partial \boldsymbol{F}_{2nof}}{\partial \boldsymbol{u}_{2nof}^T} \end{bmatrix} \begin{bmatrix} \tilde{\underline{\boldsymbol{u}}}_1 \\ \delta\tilde{\underline{u}}_x \boldsymbol{c} \\ \tilde{\boldsymbol{u}}_{2nof} \end{bmatrix} = \begin{bmatrix} \tilde{\boldsymbol{f}}_1 \\ \tilde{\boldsymbol{f}}_{2f} \\ \tilde{\underline{\boldsymbol{f}}}_{2nof} \end{bmatrix} \tag{46}$$

or:

$$\begin{bmatrix} \boldsymbol{K}_{11} & \boldsymbol{K}_{12}\boldsymbol{T} & \boldsymbol{K}_{13} \\ \boldsymbol{K}_{21} & \boldsymbol{K}_{22}\boldsymbol{T} & \boldsymbol{K}_{23} \\ \boldsymbol{K}_{31} & \boldsymbol{K}_{32}\boldsymbol{T} & \boldsymbol{K}_{33} \end{bmatrix} \begin{bmatrix} \tilde{\underline{\boldsymbol{u}}}_1 \\ \delta\tilde{\underline{u}}_x \boldsymbol{c} \\ \tilde{\boldsymbol{u}}_{2nof} \end{bmatrix} = \begin{bmatrix} \tilde{\boldsymbol{f}}_1 \\ \tilde{\boldsymbol{f}}_{2f} \\ \tilde{\underline{\boldsymbol{f}}}_{2nof} \end{bmatrix} \tag{47}$$

The boundary conditions $\tilde{\underline{\boldsymbol{u}}}_1 = \boldsymbol{0}$, $\tilde{\underline{\boldsymbol{f}}}_{2nof} = \boldsymbol{0}$, reduce the problem to:

$$\begin{bmatrix} \boldsymbol{k}_{22} & \boldsymbol{K}_{23} \\ \boldsymbol{k}_{32} & \boldsymbol{K}_{33} \end{bmatrix} \begin{bmatrix} \delta\tilde{\underline{u}}_x \\ \tilde{\boldsymbol{u}}_{2nof} \end{bmatrix} = \begin{bmatrix} \tilde{\boldsymbol{f}}_{2f} \\ \boldsymbol{0} \end{bmatrix} \tag{48}$$

where matrices vectors $\boldsymbol{k}_{22}$, $\boldsymbol{k}_{32}$ are:

$$\boldsymbol{k}_{22} = \begin{bmatrix} \sum_{i=1}^{M}(K_{22})_{1i} \\ \sum_{i=1}^{M}(K_{22})_{2i} \\ \vdots \\ \sum_{i=1}^{M}(K_{22})_{Mi} \end{bmatrix}, \quad \boldsymbol{k}_{32} = \begin{bmatrix} \sum_{i=1}^{N}(K_{32})_{1i} \\ \sum_{i=1}^{N}(K_{32})_{2i} \\ \vdots \\ \sum_{i=1}^{N}(K_{32})_{Ni} \end{bmatrix} \tag{49}$$

The generalized coordinates are:

$$\begin{bmatrix} \delta\tilde{\underline{u}}_x \\ \tilde{\boldsymbol{u}}_{2nof} \end{bmatrix} \tag{50}$$

In order to determine the generalized force, Eq. (48) is rearranged.

$$\delta\tilde{\underline{u}}_x \boldsymbol{k}_{22} + \boldsymbol{K}_{23}\tilde{\boldsymbol{u}}_{2nof} = \tilde{\boldsymbol{f}}_{2f} \tag{51}$$

The following equations are obtained by summing up the components in the

above equation as:

$$\sum_{i=1}^{M}\sum_{j=1}^{M}(K_{22})_{ij}\delta\tilde{\underline{u}}_x + \begin{bmatrix} \sum_{i=1}^{M}(K_{23})_{i1} & \cdots & \sum_{i=1}^{M}(K_{23})_{iN} \end{bmatrix} \begin{bmatrix} \tilde{u}_{2nof1} \\ \tilde{u}_{2nof2} \\ \vdots \\ \tilde{u}_{2nofN} \end{bmatrix} = \sum_{i=1}^{M}(\tilde{f}_{2f})_i \tag{52}$$

$$k_{22}\delta\tilde{\underline{u}}_x + \boldsymbol{k}_{23}^T\tilde{\boldsymbol{u}}_{2nof} = \tilde{f} \tag{53}$$

Using Eq. (53), Eq. (48) is written as:

$$\begin{bmatrix} k_{22} & \boldsymbol{k}_{32}^T \\ \boldsymbol{k}_{32} & \boldsymbol{K}_{33} \end{bmatrix} \begin{bmatrix} \delta\tilde{\underline{u}}_x \\ \tilde{\boldsymbol{u}}_{2nof} \end{bmatrix} = \begin{bmatrix} \tilde{f} \\ \boldsymbol{0} \end{bmatrix} \tag{54}$$

By transferring the known variables to the right side and the unknowns to the left, the following holds true:

$$\begin{bmatrix} k_{22}^{-1} & -k_{22}^{-1}\boldsymbol{k}_{32}^T \\ -k_{22}^{-1}\boldsymbol{k}_{32} & k_{22}^{-1}\boldsymbol{k}_{32}\boldsymbol{k}_{32}^T + \boldsymbol{K}_{33} \end{bmatrix} \begin{bmatrix} \tilde{f} \\ \tilde{\boldsymbol{u}}_{2nof} \end{bmatrix} = \begin{bmatrix} \delta\tilde{\underline{u}}_x \\ \boldsymbol{0} \end{bmatrix} \tag{55}$$

The matrix on the left is the tangent stiffness matrix, which corresponds to the case of imposed displacement.

If $\boldsymbol{\phi}_c$ is the eigenvector corresponding to the zero eigenvalue of the tangent stiffness matrix, the the following relation is considered with the vector on the right side of Eq. (55).

$$\boldsymbol{\phi}_c \cdot \begin{bmatrix} \delta\tilde{\underline{u}}_x \\ \boldsymbol{0} \end{bmatrix} = 0 \quad \Rightarrow \quad \begin{bmatrix} \delta\tilde{\underline{u}}_x \\ \boldsymbol{0} \end{bmatrix} = \sum_{i=2}^{M+N} q_i\phi_i \tag{56}$$

or

$$\boldsymbol{\phi}_c \cdot \begin{bmatrix} \delta\tilde{\underline{u}}_x \\ \boldsymbol{0} \end{bmatrix} \neq 0 \quad \Rightarrow \quad \begin{bmatrix} \delta\tilde{\underline{u}}_x \\ \boldsymbol{0} \end{bmatrix} = \sum_{i=1}^{M+N} q_i\phi_i \tag{57}$$

According to the asymptotic theory, the former is the bifurcation point and the latter the limit point.

First the former is considered and the linear equations become

$$\begin{bmatrix} k_{22}^{-1} & -k_{22}^{-1}\boldsymbol{k}_{32}^T \\ -k_{22}^{-1}\boldsymbol{k}_{32} & k_{22}^{-1}\boldsymbol{k}_{32}\boldsymbol{k}_{32}^T + \boldsymbol{K}_{33} \end{bmatrix} \left(\sum_{i=1}^{N+M} q_i\phi_i \right) = \sum_{i=2}^{N+M} \lambda_i q_i \phi_i \tag{58}$$

To satisfy this relation, an eigenvector corresponding to the zero eigenvalue is not needed. When a bifurcation occurs without any change in δu_x, the bifurcation

mode corresponding to the eigenvector of the zero eigenvalue does appear.

Considering the latter:

$$\begin{bmatrix} k_{22}^{-1} & -k_{22}^{-1}\boldsymbol{k}_{32}^{T} \\ -k_{22}^{-1}\boldsymbol{k}_{32} & k_{22}^{-1}\boldsymbol{k}_{32}\boldsymbol{k}_{32}^{T} + \boldsymbol{K}_{33} \end{bmatrix} \left(\sum_{i=1}^{N+M} q_i \phi_i \right) = \sum_{i=1}^{N+M} \lambda_i q_i \phi_i \tag{59}$$

In this case, the eigenvector must correspond to the zero eigenvalue. When a bifurcation occurs, with no change in δu_x, there is no change corresponding to the mode of the zero eigenvalue eigenvector.

This explains how to estimate the post-bifurcation path using the above tangent stiffness matrix.

3.4. Bifurcation path analysis method

3.4.1. Outline

According to section 3.2, bifurcation points are bifurcation branching points and limit points[18]. When the solution passes through a limit point, snap-through bifurcation occurs and the equilibrium path jumps in a discontinuous manner. The branching bifurcation points are classified as the symmetric and the asymmetric bifurcation points. Symmetric and asymmetric bifurcation points generate symmetric bifurcation buckling and asymmetric bifurcation buckling, respectively. It is possible to predict the type of bifurcation structure using asymptotic theory. However, the accuracy of the prediction is reduced because the higher order terms are neglected. In the case of snap-through buckling and symmetric bifurcation buckling, the direction of the incremental displacement from the buckling point is equal to the eigenvector corresponding to a zero eigenvalue. In the case of asymmetric bifurcation buckling, displacement and load should be changed to satisfy the relation in 3.2.2 (ii)-a.

At bifurcation point ($\boldsymbol{u}_c$, $\boldsymbol{f}_c$), the tangent stiffness matrix $\boldsymbol{K}$ has a zero eigenvalue $\lambda_c = 0$ ($\det\boldsymbol{K} = 0$) and a corresponding eigenvector $\boldsymbol{\phi}_c$. In order to determine the position of the bifurcation point, a pinpointing procedure that is similar to the method to solve the extended system described in Wriggers, et al.[19] is used. The eigenvalue analysis of the tangent stiffness matrix is performed and ($\boldsymbol{u}_c+\epsilon\boldsymbol{\phi}_c$, $\boldsymbol{f}_c$) is computed. The perturbed state is in the eigenvector direction from the bifurcation point, where ϵ is an infinitesimal parameter. By assuming the perturbed state is near a post-bifurcation path, a convergence calculation, the Newton-Raphson iteration, is performed as described in Section 3.2. This static analysis searches for a new equilibrium point after the bifurcation. If a post-bifurcation equilibrium point cannot be found, the initial condition is changed by varying ϵ and the search for a new equilibrium point is repeated. This method, which estimates the bifurcation mode as the eigenvector and searches for the bifurcation path, is similar to the method used in Wanger and Wriggers[13]. The difference is that Wanger and Wriggers used a directional derivative of the tangent stiffness matrix for the perturbed state. The following path analysis method algorithm has the ability to track paths after symmetric and asymmetric bifurcations, whether they are stable or unstable.

3.4.2. Analysis algorithm

If there are multiple bifurcation points with multiple zero eigenvalues, an effective way to search for buckling modes is the linear combination of eigenvectors. An algorithm to search for bifurcation solution, where the bifurcation point is a double singular point (i.e. $\boldsymbol{K}$ has two zero eigenvalues), is shown.

1. By increasing δu_x, an eigenvalue analysis of the tangent stiffness matrix $\boldsymbol{K}$ in Eq. (55) is performed.
2. Existence of the primary path is checked. For this purpose, path tracking without perturbation $\tilde{\boldsymbol{u}}$ is performed by increasing δu_x from the initial point ($\boldsymbol{u}_c$, $\boldsymbol{f}_c$).
3. The point ($\boldsymbol{u}_c + \boldsymbol{\epsilon}^T\boldsymbol{\Phi}$, $\boldsymbol{f}_c$) is calculated where the eigenvector $\boldsymbol{\phi}_1$ and $\boldsymbol{\phi}_2$ correspond to the zero eigenvalues, $\boldsymbol{\Phi} = [\boldsymbol{\phi}_1\ \boldsymbol{\phi}_2]$, $\boldsymbol{\epsilon} = [\epsilon\cos\theta\ \epsilon\sin\theta]^T$ and $0 < \epsilon \ll 1$, $0 \leq \theta < 2\pi$. Vector $\boldsymbol{\epsilon}^T\boldsymbol{\Phi}$ is called the disturbance vector. A convergence calculation for the static analysis is performed from this state to obtain a new equilibrium point. Various values of θ are tested and then ϵ is increased gradually to seek the post-bifurcation path. If the solution is obtained, the path tracking is performed by increasing δu_x from this state.
4. The point ($\boldsymbol{u} + \boldsymbol{\epsilon}^T\boldsymbol{\Phi}$, $\boldsymbol{f}$) is calculated from the pre-buckling point($\boldsymbol{u}$, $\boldsymbol{f}$), where $\boldsymbol{\epsilon}$ and $\boldsymbol{\Phi}$ are defined in step 3. If a solution is obtained, the path tracking is performed by decreasing δu_x from this point.

An algorithm for a simple singular point follows the same progression but with a slight modification. In steps 3. and 4., $\boldsymbol{u}_c \pm \epsilon\boldsymbol{\phi}$ is used instead of $\boldsymbol{u}_c + \boldsymbol{\epsilon}^T\boldsymbol{\Phi}$ where $\boldsymbol{\phi}$ is the eigenvector of the zero eigenvalue and ϵ is an infinitesimal parameter.

4. Analysis methods of solution

4.1. Symmetric solutions

Based on group theory[20], the equivalence of a system that possesses symmetry is described as:

$$\boldsymbol{M}(\gamma)\boldsymbol{f}(\boldsymbol{u}(\boldsymbol{x}), \mu) = \boldsymbol{f}(\boldsymbol{M}(\gamma)\boldsymbol{u}(\boldsymbol{M}(\gamma)\boldsymbol{x}), \mu) \tag{60}$$

where $\boldsymbol{M}(\gamma)$ is the representation matrix of a group element γ. A group element is defined as $\gamma : f_1 \mapsto f_2$.

The observed membrane has symmetry that is invariant with respect to e, s, r and sr, where e is the identity transformation, s is the reflection transformation with respect to xy-plane, r is the rotation transformation by 180° about the z-axis and sr is the combination of s and r. This symmetry group is known as the dihedral group $D_2 = \{e, r, s, sr\}$. The representation matrices for the elements

are:

$$\boldsymbol{M}(e) = \begin{bmatrix} 1 & 0 & 0 \\ 0 & 1 & 0 \\ 0 & 0 & 1 \end{bmatrix}, \qquad \boldsymbol{M}(r) = \begin{bmatrix} -1 & 0 & 0 \\ 0 & -1 & 0 \\ 0 & 0 & 1 \end{bmatrix}$$
$$\boldsymbol{M}(s) = \begin{bmatrix} 1 & 0 & 0 \\ 0 & 1 & 0 \\ 0 & 0 & -1 \end{bmatrix}, \qquad \boldsymbol{M}(sr) = \begin{bmatrix} -1 & 0 & 0 \\ 0 & -1 & 0 \\ 0 & 0 & -1 \end{bmatrix} \tag{61}$$

The rotation transformation is a 180° rotation about z-axis at the origin in Fig. 1. Substituting them into the governing equations (4) yields:

$$\boldsymbol{f}(\boldsymbol{M}(r)\boldsymbol{u}(\boldsymbol{M}(r)\boldsymbol{x})) = [-f_x,\, -f_y,\, f_z]^T = \boldsymbol{M}(r)\boldsymbol{f}(\boldsymbol{u}(\boldsymbol{x})) = \boldsymbol{0} \tag{62}$$
$$\boldsymbol{f}(\boldsymbol{M}(s)\boldsymbol{u}(\boldsymbol{M}(s)\boldsymbol{x})) = [f_x,\, f_y,\, -f_z]^T = \boldsymbol{M}(s)\boldsymbol{f}(\boldsymbol{u}(\boldsymbol{x})) = \boldsymbol{0} \tag{63}$$
$$\boldsymbol{f}(\boldsymbol{M}(sr)\boldsymbol{u}(\boldsymbol{M}(sr)\boldsymbol{x})) = [-f_x,\, -f_y,\, -f_z]^T = \boldsymbol{M}(sr)\boldsymbol{f}(\boldsymbol{u}(\boldsymbol{x})) = \boldsymbol{0} \tag{64}$$

Hence, the symmetry transformations satisfy the equivalence condition of the governing equations. In addition, the boundary conditions in Eqs. (5) to (9) are invariant under the symmetry transformations. As a result, this system has the symmetry that is invariant under all possible transformations.

Deformation $\boldsymbol{u}_0(x,\, y,\, z)$ satisfies the governing equations (4) and boundary conditions of Eqs. (5) to (9). Three deformations $\boldsymbol{u}_s(x,\, y,\, z)$, $\boldsymbol{u}_r(x,\, y,\, z)$, and $\boldsymbol{u}_{sr}(x,\, y,\, z)$ are obtained from $\boldsymbol{u}_0(x,\, y,\, z)$ by means of the reflection transformation, the rotation transformation, and the rotation and reflection transformation, respectively. The three deformations $\boldsymbol{u}_s$, $\boldsymbol{u}_r$, and $\boldsymbol{u}_{sr}$ are the solutions satisfying the governing equations (4) and the boundary conditions of Eqs. (5) to (9).

Symmetry between two solutions is defined through an example. If deformation $\boldsymbol{u}_1(x,\, y,\, z)$ is equivalent to $\boldsymbol{u}_{sr}(x,\, y,\, z)$, there exists a symmetry where $\boldsymbol{u}_0$ agrees with $\boldsymbol{u}_1$ using the rotation and reflection transformation. Also, $\boldsymbol{u}_1$ is equivalent to $\boldsymbol{u}_0$ transformed by the rotation and reflection transformation. In other words, $\boldsymbol{u}_0$ and $\boldsymbol{u}_1$ have the rotation and reflection symmetry.

Symmetry in a solution can also be defined through an example. If $\boldsymbol{u}_0(x,\, y,\, z)$ is equivalent to $\boldsymbol{u}_r(x,\, y,\, z)$, then $\boldsymbol{u}_0$ has the symmetry that is invariant under the rotation transformation.

The above relations can be viewed in two ways. First, a specific deformation is obtained by symmetry transformation from another deformation. Second, two different deformations are equivalent by a symmetry transformation. In the second case, it is said that the deformations are different representations of a single wrinkle pattern.

4.2. Translation symmetry

It is assumed that the solution $\boldsymbol{u}_0(x,\, y,\, z)$ satisfies the governing equation (4) and the boundary conditions in Eqs. (5) to (9). By translating $\boldsymbol{u}_0$ in x-

direction by Δx, a displacement $\boldsymbol{u}_t$ is obtained.

$$\boldsymbol{u}_t(x,\,y,\,z) = \begin{cases} \boldsymbol{u}_0(x-\Delta x,\,y,\,z) & (-\frac{a}{2} \le x-\Delta x \le \frac{a}{2}) \\ \boldsymbol{u}_0(x-\Delta x+a,\,y,\,z) & (x-\Delta x < -\frac{a}{2}) \end{cases} \tag{65}$$

Here, Δx satisfies $0 \le \Delta x < a$. The translation $\Delta x \pm na$ where $(n = 1,\,2,\,\ldots)$ can be considered as the translation Δx.

Because $\boldsymbol{u}_0(x,\,y,\,z)$ satisfies the governing equations, $\boldsymbol{f}(\boldsymbol{u}_0(x,\,y,\,z)) = \boldsymbol{0}$, the following holds true:

$$\boldsymbol{f}(\boldsymbol{u}_t(x,\,y,\,z)) = \boldsymbol{0} \tag{66}$$

Therefore, the displacement $\boldsymbol{u}_t(x,\,y,\,z)$ is also a solution to the governing equations. The $\boldsymbol{u}_t(x,\,y,\,z)$ of $x \le a/2$ corresponds to $\boldsymbol{u}_0(x,\,y,\,z)$ of $x \le a/2 - \Delta x$ because $\boldsymbol{u}_t$ is obtained by translating $\boldsymbol{u}_0$ in the x-direction by Δx. In turn, $\boldsymbol{u}_t(x,\,y,\,z)$ of $x \ge -a/2$ corresponds to $\boldsymbol{u}_0(x,\,y,\,z)$ of $x \ge a/2 - \Delta x$. Therefore, the cyclic boundary conditions of $\boldsymbol{u}_t(x,\,y,\,z)$ at $x = \pm a/2$ are naturally satisfied. From the above, it is clear that $\boldsymbol{u}_t(x,\,y,\,z)$, which is obtained by a translation of $\boldsymbol{u}_0(x,\,y,\,z)$ in the x-direction by Δx, also satisfies the governing equations and boundary conditions.

In addition, it can be said that the solution $\boldsymbol{u}_t(x,\,y,\,z)$ is a symmetric with respect to $\boldsymbol{u}_0(x,\,y,\,z)$ by translation of Δx in the x-direction. In the following discussions, the two solutions are not considered as essentially different. In addition, Δx can be any arbitrary value, resulting in an infinite number of solutions $\boldsymbol{u}_t(x,\,y,\,z)$ obtained by translation of $\boldsymbol{u}_0(x,\,y,\,z)$. These infinite number of solutions are identified by translational symmetry and are represented by only $\boldsymbol{u}_0$.

4.3. Translation transformation calculation

Since there are an infinite number of translations of a specific solution, a problem is to identify the value of translation value between two solutions obtained by the analysis. An approach used in image processing[21] is useful for this purpose. The solution of a FEM analysis is represented by node values resulting in a finite set of values whose size is $N_x \times N_y$. To determine the translation value between two finite sets, the phase correlation between the two sets is calculated as:

$$R(m,\,n) = \frac{\hat{f}_1(m,n)\hat{f}_2^*(m,\,n)}{|\hat{f}_1(m,\,n)\hat{f}_2^*(m,\,n)|} \tag{67}$$

$$= e^{i\frac{2\pi}{N_x}m(\Delta n_x - 1)} e^{i\frac{2\pi}{N_y}n(\Delta n_y - 1)} \tag{68}$$

where $\hat{f}_i$ is a Fourier transform of a finite set f_i representing a solution $\boldsymbol{u}_i(x,\,y,\,z)$, $\hat{f}_2^*$ indicates the complex conjugate of $\hat{f}_2$ and Δn_x and Δn_y are discrete translations in respective directions. The phase correlation product $R(m,\,n)$ represents the inner product between individual frequencies that represent the two solutions. By taking the inverse transform $r(\Delta n_x, \Delta n_y) = \mathscr{F}^{-1}\{R(m,\,n)\}$ we form

a function represented in the $(\Delta n_x, \Delta n_y)$ domain and whose value indicates the inner products of two solutions for that specific translation value.

The cyclic boundary conditions allow movement in only x-direction, therefore $\Delta n_y \equiv 0$. This results in a one-dimensional problem to find the highest value of r for Δn_x corresponding to the best similarity.

Considering the original discrete solution, the resolution, the minimum value of the above described translational displacement is a/N_x. However, the solutions representing deformation are continuous in reality. For the continuous solutions, the transversal displacement that results in best matching is not discrete. In order to obtain a larger resolution, the following calculation is performed. Using the FEM nodal displacements, a continuous function representing the deformation is constructed as a Fourier series. From the continuous function, a new set of discrete values is constructed by sampling of sub-node positions. By increasing the number of points considered as M_x, where $M_x > N_x$, the resolution of translation becomes larger. In y direction the resolution stays the same because the translation is always 0.

4.4. Similarity value

In order to identify similarity between the two solutions, the similarity value is constructed as the inner product of solutions:

$$< f_1(n_x, n_y),\, f_2(n_x, n_y) >= \sum_{p=1}^{N_x} \sum_{q=1}^{N_y} \hat{f}_1(m, n) \hat{f}_2^*(m, n) \tag{69}$$

where $f_j(n_x, n_y)$ is a vector whose components are displacement values sampled at all finite element nodes and $\hat{f}_j(m, n)$ is the discrete Fourier transformation of $f_j(n_x, n_y)$.

The similarity value is evaluated using the first bifurcation point of the membrane. Because of membrane symmetry, the first bifurcation point is also symmetric, as is theoretically predicted. Therefore, the theoretical similarity value between two deformations should be 1. However, the above defined similarity value is based on a discrete set. When the similarity value of f_1 and f_2 are obtained numerically after the first bifurcation point, a value of 0.999995... was obtained. Therefore, the values after the fifth digit are considered to be numerical error. During comparison of different deformations, the number of digits to which similarity is obtained is referred, e.g. 0.99999345 achieved similarity within 5 digits.

4.5. Bifurcation diagram

A method of expressing the equilibrium path as it passes through the bifurcation point is needed. Here, calculating the inner product of the eigenvector and the incremental displacement vector is considered to make a bifurcation diagram.

At the bifurcation point ($\boldsymbol{u}_c$, $\boldsymbol{F}_c$), the tangent stiffness matrix $\boldsymbol{K}_c$ becomes $\det \boldsymbol{K}_c = 0$. At this point there exist N_c zero eigenvalues $\lambda_{ci} = 0$ $(i = 1, \ldots, N_c)$ and corresponding eigenvectors $\boldsymbol{\phi}_{ci}$.

$$\boldsymbol{K}_{ci}\boldsymbol{\phi}_{ci} = \lambda_{ci}\boldsymbol{\phi}_{ci} \quad (i = 1, 2, \ldots, N_c)$$

where $\boldsymbol{\phi}_{ci}$ is normalized as $||\boldsymbol{\phi}_{ci}|| = 1$. Using $\lambda_{ci} = 0$ and where c_i is an arbitrary constant results in:

$$\boldsymbol{K}_c \left(\sum_{i=1}^{N_c} c_i \boldsymbol{\phi}_{ci} \right) = \boldsymbol{0} \tag{70}$$

As explained in the earlier section the incremental displacement $\tilde{\boldsymbol{u}}_c$ occurs whereas the incremental load $\tilde{\boldsymbol{f}} \simeq \boldsymbol{0}$:

$$\boldsymbol{K}_c \tilde{\boldsymbol{u}}_c \simeq \boldsymbol{0} \tag{71}$$

Combining Eq. (70) and Eq. (71) the following holds:

$$\tilde{\boldsymbol{u}}_c \simeq \sum_{i=1}^{N_c} c_i \boldsymbol{\phi}_{ci} \tag{72}$$

The displacement increment after the bifurcation point, $\tilde{\boldsymbol{u}}$ is expressed as a linear combination of eigenvectors $\boldsymbol{\phi}_{ci}$ corresponding to the zero eigenvalues of the tangent stiffness matrix. Calculation of c_i is as:

$$c_i = \tilde{\boldsymbol{u}}_c \cdot \boldsymbol{\phi}_{ci} \ (i = 1, \ldots, N_c) \tag{73}$$

For construction of the bifurcation diagram, c_i will be used.

5. Numerical results

5.1. Validity of the FEM modeling

Experimental confirmation of behavior in cyclic boundary membranes is not possible. However, experimental data is available for the same membrane model where cyclic boundaries were replaced with free boundaries[4]. Therefore, the geometry, membrane properties, and boundary conditions mentioned in section 2 are compared and FEM model accuracy is tested. Based on discussions in Wong and Pellegrino[6], the S4R (4 node shell element with reduced Gauss integration) elements are selected. Using this element, numerical results agree best with the experimental results in Wong and Pellegrino[4] and Inoue[17]. The number of elements is $360 \times 120 = 4.23 \times 10^4$, which is the same value used in Wong and Pellegrino[6] for a membrane with an aspect ratio of 3:1. By maintaining the elements square shaped, the number of elements can be increased or decreased by changing the number of elements along a single edge of the membrane, where the other edge is determined by the aspect ratio.

By increasing the shear displacement up to $\delta u_x = 250 \times 10^{-6}$[m], the wavelength and amplitude of wrinkles are observed as indicators of wrinkle shape at at section AA'. Because of the free boundaries, the wrinkle amplitude and wavelength near those boundaries varies by a large amount. By omitting the first 6 wrinkles from each free boundary, the amplitude and wavelength average of the remaining wrinkles is more closer to the individual values. Fig. 2 a) shows the convergence of wavelength with respect to the number of elements in the FE model. Thus, the element number $360 \times 120 = 4.23 \times 10^4$ achieves sufficient convergence. A larger number of elements would increase the computational cost with minimum improvements wavelength accuracy. The amplitude convergence is similar and omitted.

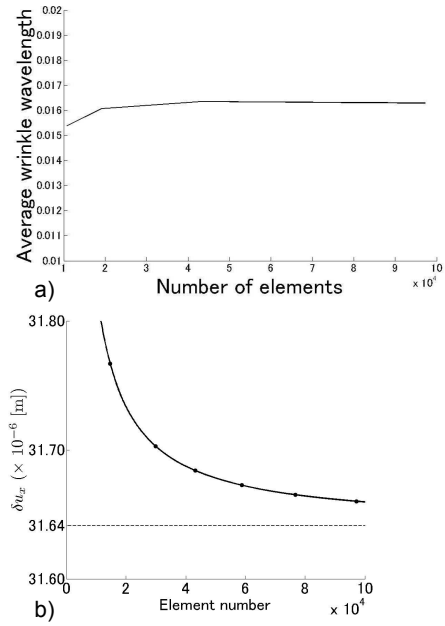

Figure 2: Convergence: a) wrinkle wavelength with element number, and b) δu_x at the first bifurcation point with element number.

When compatibility and completeness conditions are satisfied, an asymptotic convergence toward the continuum model is obtained by increasing the number of elements. Considering the problem of this study, the shear displacement δu_x needed for the first bifurcation point is analyzed with respect to the mesh density. The dots in Fig. 2 b) are obtained by this analysis, and a function $y = a_1 x^{-2} + a_2 x^{-1} + a_3$ is used to connect them. The convergence indicates that the bifurcation point is located at 31.64×10^{-6} [m]. As can be seen, the FEM model with $360 \times 120 = 4.32 \times 10^4$ elements has a relative error of 0.13 %. The conclusion is that sufficient convergence has been obtained.

More element numbers, e.g. 375×125, 390×130, and 432×144 were also

used for analysis. The results from these numbers of elements were compared to the result from 360×120 elements to confirm that the results converged and were insensitive above 4.32×10^4 elements. This also applies to results for $\delta u_x > 250 \times 10^{-6}$[m].

The convergence of the numerical results is controlled by two additional parameters in the ABAQUS calculation. First, R_n^α is the convergence criterion for the ratio of the largest residual to the corresponding average flux norm. The default value is $R_n^\alpha = 5 \times 10^{-3}$. Second is C_n^α, which is the convergence criterion for the ratio of the largest solution correction to the largest corresponding incremental solution value. Its default value is $C_n^\alpha = 1 \times 10^{-2}$. For general analysis, the default values are sufficient; however, to obtain more precise results, values that are 10^{-4} times of the default values are used combined with the δu_x increment of 10^{-7}[m].

5.2. 3:1 Free boundary membrane behavior

The rectangular free boundary membrane is a typical membrane model used in experiments that focus on membrane wrinkling. The model uses the same geometry and material properties as the 3:1 cyclic boundary membrane defined in section 2. The cyclic boundaries are replaced by free boundaries. The behavior is analyzed using the analysis method described in section 3.4.

5.2.1. Generation of a 34 wrinkle pattern

The shear displacement δu_x is gradually increased for the $0 \leq \delta u_x < 80.48 \times 10^{-6}$ [m] interval. Detail behavior for this interval is given in Senda, et al. [22]. Here a summary will be given. At $\delta u_x = 31.68 \times 10^{-6}$ [m], the first bifurcation point generates 7 wrinkles near each free boundary, resulting in a 14 wrinkle pattern. By increasing δu_x, the number of wrinkles gradually increases. After a bifurcation point at $\delta u_x = 80.48 \times 10^{-6}$ [m], the membrane is fully wrinkled as shown in Fig. 6 a). Due to free boundaries, the variation in wrinkle shape along the length of the membrane can be observed.

5.2.2. Collapsed section generation

After the bifurcation point at $\delta u_x = 80.48 \times 10^{-6}$ [m], path tracking is performed for the interval $80.48 \times 10^{-6} \leq \delta u_x < 440.21 \times 10^{-6}$[m], as shown in Fig. 6. By increasing δu_x, the wrinkle amplitude decreases locally near the fixed boundaries, resulting in curvature inflections. Further increase in δu_x results in a section of a wrinkle with out-of-plane displacement of opposite sign than the rest of the wrinkle.

Additionally, a shift in collapsed section position is observed. Both amplitude changes and position shifts occur while all eigenvalues of the tangent stiffness matrix remain positive. Therefore, this behavior occurs without bifurcations.

Figures 9 and 10 show the first principal stress, σ_ξ and the second principal stress, σ_η, respectively. The values are observed at $\delta u_x = 90.00 \times 10^{-6}$[m]. The majority of collapsed sections occur in the region of high tensile σ_ξ and

high compressive σ_η. However, near the free boundaries, both the tension and compression start to fall off. Therefore, it is difficult to determine in which region the collapsed sections originate. By replacing free boundaries with cyclic boundaries, in the later sections it will be shown that the collapsed sections originate in regions of high tensile σ_ξ and high compressive σ_η.

5.2.3. Wrinkle generation

At $\delta u_x = 440.21 \times 10^{-6}$[m], the collapsed sections of two wrinkles reach critical sizes. The result is a bifurcation point where one of the two wrinkles split and two new wrinkles are generated.

In Fig. 7, the behavior at this point can be observed. The initial out-of-plane deformation at $\delta u_x = 440.21 \times 10^{-6}$[m], before the disturbance vector imposition, is observed in Fig. 7 a). The disturbance vector imposition causes a snap through bifurcation. The initial deformation jumps to one of the patterns observed in Fig. 7 b) and c). The collapsed sections near the top and bottom fixed boundaries of one wrinkle expand toward the middle of the wrinkle. By increasing shear to $\delta u_x = 440.50 \times 10^{-6}$[m], the generation of new wrinkles is finalized. Figure 7 b) and c) respectively become Fig. 7 d) and e). The expanded collapsed sections meet, and the wrinkle amplitude along the center drops until it changes its sign. One wrinkle is replaced by three wrinkles, two of the same sign and one wrinkle of the opposite sign. The collapsed sections on other wrinkles remain after the bifurcation.

Additional shear increases the size of remaining collapsed sections. The next bifurcation point is at $\delta u_x = 645.96 \times 10^{-6}$[m] where the same process occurs. The out-of-plane deformation at $\delta u_x = 645.96 \times 10^{-6}$[m], before the disturbance vector imposition, is shown in Fig. 8 a). Collapsed sections near the top and bottom fixed boundaries expand toward the middle of the wrinkle as in Fig. 8 b) and c). By slight increase in shear to $\delta u_x = 646.00 \times 10^{-6}$[m], Fig. 8 b) and c) respectively, become Fig. 8 d) and e) and the wrinkle generation is completed.

It can be concluded that collapsed sections are the cause of new wrinkle generation. Essentially, small wrinkles expand and generate larger wrinkles. However, the lack of wrinkle uniformity due to free boundaries makes the observation of collapsed sections inconsistent. As was seen in the results, collapsed sections on wrinkles near the free boundaries have a large variation of shapes. The positioning of collapsed sections is also different from wrinkle to wrinkle. A collapsed section along the middle of a wrinkle may split a wrinkle at smaller values of shear than a collapsed section that is along the side of a wrinkle. Therefore, additional analysis without effects of free boundaries is needed to clearly explain collapsed section behavior.

5.3. Cyclic boundary membrane behavior

In the previous section, the behavior where collapsed sections cause wrinkle generation was shown. This may be a fundamental mechanism to generate new wrinkles when the membrane is fully wrinkled. However, the shape of wrinkles and collapsed sections is affected by the existence of free boundaries. Therefore,

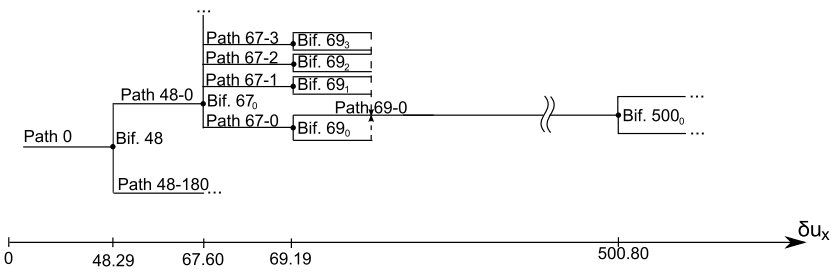

Figure 3: 3:1 cyclic membrane schematic bifurcation diagram

the universality of the wrinkle generation mechanism may be affected. In order to eliminate the effects of free boundaries, cyclic boundaries are introduced, and the fundamental behavior can be observed.

In this section, the behavior of the cyclic boundary membranes will be shown. The schematic bifurcation diagram is shown in Fig. 3. The diagram shows the positioning of bifurcation points and paths that lead to and from those bifurcation points. For notation, bifurcation points are indicated by 'Bif. X_n', where X indicates the micrometer value of the δu_x where the bifurcation point occurs. The subscript n is an identifier used if there are multiple bifurcation points at the same value of δu_x. Paths are indicated by 'Path Y-m', where Y is the value of the δu_x where the path starts, and m is an identifier indicating the value of θ for which the path was obtained, as discussed in section 3.4.2.

Because of membrane symmetry, only a small part of the total bifurcation structure is shown. The translation symmetry is achieved for any arbitrary value of translation, resulting in infinite many paths representing a single unique wrinkle pattern. Therefore, only the original path is drawn. The analysis for the membrane shows the behavior for $0 \leq \delta u_x \leq 510.00 \times 10^{-6}$[m].

5.3.1. Bif. 48

The initial condition is a flat membrane. First, tension $\delta u_y = 30 \times 10^{-6}$[m] is applied in the y-direction and maintained constant throughout the analysis. Then, increasing δu_x results in a tensile first principal stress and a compressive second principal stress. Once the second principal stress reaches a critical value, the first bifurcation occurs.

The first bifurcation occurs at $\delta u_x = 48.29 \times 10^{-6}$[m] as Bif. 48. This bifurcation generates 32 wrinkles, i.e. 16 convex up and 16 convex down wrinkles. The out-of-plane deformation for the membrane is shown in Fig. 11 a). Figure 11 b) shows the out-of-plane deformation for section BB'. As indicated by the figures, all wrinkles have the same shape. As a result, the deformation that is translated by an integer number of wrinkle wavelength is equivalent to the original deformation. Hence, this deformation has the symmetry that is invariant under the translation transformation by $na/16$ ($n = \pm 1, \pm 2, \ldots$) in x-direction.

The bifurcation structure of Bif. 48 is shown in Fig. 12 a). The structure is a

symmetric bifurcation. As a result, wrinkles rapidly increase in amplitude from a flat membrane after the bifurcation. The paths are calculated by considering θ at increments of 30°. However, a path can be obtained for any θ. The disturbance vector is constructed from two orthogonal eigenvectors, and the disturbance vector of $\theta = 0°$ is translated in x-direction in accordance with θ. Hence, a path obtained for a certain θ represents a path that is obtained from the path of $\theta = 0°$ by translating in x-direction.

There are Path 48-0 and Path 48-180 after Bif. 48 in Fig. 3 because this is a symmetry bifurcation point. Because the deformation patterns of Path 48-0 and Path 48-180 have the reflection symmetry, there is only one wrinkle pattern after Bif. 48. A single path, Path 48-0, defined by $\theta = 0°$ is tracked by increasing δu_x.

5.3.2. Bif. 67

On Path 48-0, the membrane has 32 wrinkles with same shape. Increasing δu_x results in wrinkle amplitude augmentation. The second bifurcation occurs at $\delta u_x = 67.60 \times 10^{-6}$[m] as Bif. 67_0. The out-of-plane deformation of the membrane is shown in Fig. 13 a). Figure 13 b) shows the out-of-plane deformation on section BB'. For Path 48-0, the deformation is a sinusoidal shape with a period of $a/16$ in x-direction and a mean of zero. After the bifurcation, a variation of the mean in the form of a sinusoidal deformation with a period of $a/2$ in x-direction is observed on section BB'. While the variation is observed near the fixed boundaries, it is not observed in the middle of the membrane on section AA'.

The bifurcation structure for Bif. 67 is shown in Fig. 12 b). Paths are obtained for values of θ from 0° to 360° for every 22.5°. Figure 12 c) shows paths for θ from 0° to 22.5°.

A single group is defined for the θ range of 22.5°. This is due to the sinusoidal deformation of period $a/2$ being imposed onto the base sinusoidal deformation of period $a/16$. The value of θ defines the x-direction position of the $a/2$ period sinusoidal shape. Considering that the full range of imposition of θ is 360°, the period of $a/16$ in x defines the range of a group as $360°/16 = 22.5°$.

For a given θ, an equilibrium path will be produced where the peaks of the $a/2$ period sinusoidal deformation produce two wrinkles with larger amplitude values. As indicated by Fig. 3, there are many paths leading form Bif. 67_0. However, the paths do not exist only for discrete values of θ as the figure suggests, but for any arbitrary value. This results in an infinite number of paths generated at Bif. 67_0. Any two paths in a group have different deformation shapes when their θ values are not same.

By considering a path in group 1 defined as $\theta = \theta'$, any group n path defined as $\theta = \theta' + n \times 22.5°$ will have a 5 digit similarity with the group 1 path after a translation transformation by $n\,a/16$. This means that groups represent sets of deformation that are equivalent with translation symmetry. Therefore, only paths of one group will be tracked until the next bifurcation.

5.3.3. Bif. 69

On any Path 67, the membrane has 32 wrinkles where two wrinkles have slightly larger amplitudes. By increasing δu_x, the wrinkle amplitude increases. The third bifurcation occurs at $\delta u_x = 69.19 \times 10^{-6}$[m] as Bif. 69. This is a symmetric snap through bifurcation. The out-of-plane deformation after this bifurcation is shown in Fig. 14 a). Figure 14 b) shows the deformation in section BB'. The number of wrinkles increases by 2 resulting in a 34 wrinkle pattern. All wrinkles in this pattern have the same shape. As a result, this deformation has the symmetry that is invariant under the translation transformation by $na/16$ $(n = \pm 1, \pm 2, \ldots)$ in x-direction.

The bifurcation structure for Bif. 69 is shown in Fig. 12 d). As can be seen, there are two paths leading from the bifurcation point. The wrinkle generation occurs during an unstable split of one of the existing wrinkles. Two wrinkles are candidates for splitting. They correspond to the two wrinkles with slightly larger amplitudes. Therefore, each of the paths after the bifurcation represent one of the wrinkles that splits.

Comparison among all paths generated at Bif. 69, based on all paths of a single group from Bif. 67, results in 5 digit similarity. Also, the comparison between individual wrinkles for one wrinkle pattern shows that all wrinkles are the same. Therefore, the conclusion is that after Bif. 69 there exists a single unique wrinkle pattern but an infinite number of equilibrium paths. All these paths correspond to translation transformations in x-direction of the unique wrinkle pattern. Because of this, only one path is selected for tracking.

5.3.4. Path 69-0

Path 69-0 is the selected path after Bif. 69 and it contains 34 wrinkles that have the same shape. The following behavior observed occurs at regular equilibrium points. The tangent stiffness matrix remains positive definite until the next bifurcation.

Path 69-0 is observed for $69.19 \times 10^{-6} \leq \delta u_x \leq 500.80 \times 10^{-6}$[m]. By increasing δu_x, collapsed sections are generated near the fixed boundaries on existing wrinkles. Figure 15 b) show the deformation for section BB' at $\delta u_x = 85.00 \times 10^{-6}$[m]. The collapsed sections can be observed as a local decrease in wrinkle amplitude near the fixed boundaries.

By increasing δu_x, these sections grow in size and number. Figures 15 c) and d) show the collapsed section at $\delta u_x = 500.00 \times 10^{-6}$[m]. The existence of these collapsed sections resulted in all wrinkles having different shapes, where previously all wrinkles were the same shape.

5.3.5. Bif. 500

The later part of Path 69-0 is a membrane that contains collapsed section on existing wrinkles. The fourth bifurcation occurs at $\delta u_x = 500.80 \times 10^{-6}$[m] as Bif. 500. The bifurcation is a snap through bifurcation where three wrinkles split and generate six new wrinkles. The out-of-plane deformation is shown in Fig. 16. Figure 16 b) shows the deformation on section BB'. The result of the bifurcation is a 40 wrinkle pattern.

The process of wrinkle generation can be observed in Fig. 17. The membrane starts as in Fig. 17 a). The largest collapsed sections are destabilized. A section will rapidly expand along the length of the wrinkle until it meets with the opposite collapsed section in the middle. The affected wrinkles start to split as in Fig. 17 c). The split is then finalized as in Fig. 17 d). The collapsed sections on the other wrinkles remain.

It can be concluded that after about $\delta u_x \approx 80 \times 10^{-6}$[m], the behavior of the cyclic boundary membrane is similar to that of the free boundary membrane. Collapsed sections are generated near the fixed boundaries, and as shear is increased, the sections increase in size. At a specific value of shear, they destabilize the large wrinkle and split it in half. Therefore, it can be concluded that the free boundaries are not essential in collapsed section formation.

5.4. Generation of collapsed sections

As was shown in the results, there exist stable equilibrium paths without bifurcation points, where small wrinkles or collapsed sections are generated. To understand this behavior, the wrinkle geometry and membrane equilibrium are observed near the fixed boundaries. The geometry of a single wrinkle is shown

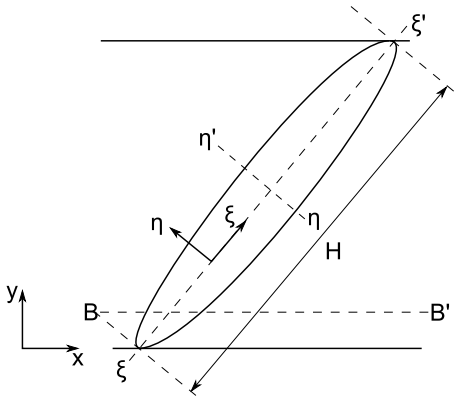

Figure 4: Wrinkle geometry.

in Fig. 4. The behavior of collapsed sections is observed in two stages. The first stage is a local decrease in wrinkle amplitude and the second stage is the curvature sign change. Both stages can be observed in the interval $70.0 \times 10^{-6} \leq \delta u_x \leq 82.0 \times 10^{-6}$ [m].

After Bif. 69, a wrinkle pattern consists of 34 sinusoidal wrinkles as shown in Fig. 14. The first principal stress, σ_ξ is shown in Fig. 19. The second principal stress, σ_η is shown in Fig. 20. The stress state for the entire membrane is tension and compression. The first principal stress, σ_ξ, has the highest value in the middle of the membrane and falls off slightly toward the fixed boundaries. The second principal stress, σ_η, has the smallest value near the fixed boundaries and increases toward the middle of the membrane.

First the interval $70.0 \times 10^{-6} \leq \delta u_x \leq 74.0 \times 10^{-6}$ [m] is observed on sections $\xi\xi'$ and $\eta\eta'$. Definition of the sections $\xi\xi'$ and $\eta\eta'$ is shown in Fig. 18. The position on the section is defined by node values based on the finite element nodes. Figures 21 and 22 show the principal stress values on section $\xi\xi'$. As δu_x is increased, the first principal stress increases for the entire section. The second principal stress decreases, however the change is small compared the total value.

Figure 23 shows the out-of-plane displacement, u_z, on section $\xi\xi'$. Figure 24 shows the curvature, $\partial^2 u_z/\partial\xi^2 = \kappa_\eta$, on section $\xi\xi'$. Figure 25 shows the out-of-plane displacement, u_z, on section $\eta\eta'$. Figure 26 shows the curvature, $\partial^2 u_z/\partial\eta^2 = \kappa_\xi$, on section $\eta\eta'$. The sections cross each other at node 15 of section $\xi\xi'$, and node 9 of section $\eta\eta'$. For the interval $70.0 \times 10^{-6} \leq \delta u_x \leq 72.0 \times 10^{-6}$ [m], the increasing δu_x increases the wrinkle amplitude for the entire section. At $\delta u_x = 73.0 \times 10^{-6}$ [m], a drop in amplitude is observed between nodes 1 and 32, while an increase is observed after node 32. The curvature κ_ξ in Fig. 26 shows that while the amplitude decreases, the wrinkle maintains a convex up shape along η. The curvature κ_η in Fig. 24 is positive between nodes 1 and 7, and increases for interval $70.0 \times 10^{-6} \leq \delta u_x \leq 72.0 \times 10^{-6}$ [m]. However, for $\delta u_x = 73.0 \times 10^{-6}$ [m] it starts dropping. For nodes after node 7, the curvature κ_η is negative with a minimum value at node 11. For the interval $70.0 \times 10^{-6} \leq \delta u_x \leq 72.0 \times 10^{-6}$ [m], the minimum value decreases. However, it increases for $\delta u_x = 73.0 \times 10^{-6}$ [m].

Next, the interval $74.0 \times 10^{-6} \leq \delta u_x \leq 82.0 \times 10^{-6}$ [m] is observed. The principal stress behavior is the same as before; both tension and compression increase. Figure 29 shows the out-of-plane displacement, u_z, on section $\xi\xi'$. Figure 30 shows the curvature, κ_η, on section $\xi\xi'$. Figure 31 shows the out-of-plane displacement, u_z, on section $\eta\eta'$. Figure 32 shows the curvature, κ_ξ, on section $\eta\eta'$. As δu_x increases, amplitude up to node 32 continues decreasing. As a result, the curvature, κ_η, also approaches 0. At $\delta u_x = 76.0 \times 10^{-6}$ [m], the decrease in wrinkle amplitude reached the point where the wrinkle becomes flat in the η-direction as seen in Figs. 31 and 32. At the flat top of the wrinkle, it can be observed that both κ_η and κ_ξ are almost 0. The amplitude drops further and a convex up wrinkle gains a convex down peak. At this point both curvature κ_η and κ_ξ change their signs.

Following the discussion about thin plate bending in Timoshenko[3], the equilibrium of a plate element in z-direction can be written as

$$\frac{\partial Q_\xi}{\partial \xi} + \frac{\partial Q_\eta}{\partial \eta} = N_\xi \kappa_\eta + N_\eta \kappa_\xi \tag{74}$$

The left side of the above expression represents the bending of the plate due to transversal forces Q, while the right side represents the membrane behavior due to mid-plane forces N. The mid-plane forces N_ξ and N_η are obtained by integration of principal stress values over the membrane thickness. The values can be approximated as $N_\xi = h\sigma_\xi$ and $N_\eta = h\sigma_\eta$ where h is the membrane thickness. The transversal forces are obtained in Fig. 33 as Q_ξ and in Fig. 34 as Q_η. At the fixed boundary, the transversal forces correspond to the reaction

forces from the boundary. By moving away from the fixed boundary, both Q_ξ and Q_η increase rapidly toward 0. After node 8 of the $\xi\xi'$ section and node 11 of the $\eta\eta'$ section the values become almost constant. By observing the equilibrium equation, it can be concluded that very near the fixed boundaries, the membrane behavior is determined by both transversal and mid-plane forces. In other words, the membrane behaves as a thin plate. By moving away from the fixed boundaries, the effects of transversal forces fall off and the behavior is mostly determined by mid-plane forces. Therefore, the left side of Eq. (74) is approximately zero, and the equation becomes a membrane equilibrium.

Near the the fixed boundaries, positive σ_ξ over positive κ_η results in an upward force. The negative σ_η over negative κ_ξ also results in an upward force. The equilibrium is maintained by the downward transversal forces near the fixed boundaries, due to the bending stiffness of the membrane. Because of the bending stiffness and the boundary conditions, κ_η is positive and out-of-plane displacement is inhibited.

When a flat membrane is considered, positive σ_ξ and negative σ_η correspond to the extension of membrane length along ξ-direction and the reduction of membrane length along η-direction. In addition, σ_ξ and σ_η are generally proportional to δu_x and constant throughout the membrane. However, in the actual membrane, out-of-plane deformation has occurred, which results in Figs. 19 to 26.

As shown in Figs. 19 and 21, there is only a small percentage difference in σ_ξ between the values in the middle of the membrane and near the fixed boundaries. As δu_x is increased, the length of the membrane along ξ-direction increases, resulting in higher values of σ_ξ.

As shown in Figs. 20 and 22, there is an order of one difference in σ_η magnitude between the values in the middle of the membrane and near the fixed boundaries. After node 20, with increasing δu_x there is no significant change in σ_η, meaning there is no significant reduction in membrane length. As indicated by Fig. 23, the reduction in length along η-direction does not occur because the wrinkle amplitude is increased which releases the stress. However, by approaching the fixed boundaries, the increase in δu_x results in an increase in compression, meaning there exists a reduction in length along the η-direction. This is because the fixed boundaries limit the increase in amplitude and prevent the release of stress.

Additional increase in δu_x is shown in Figs. 27 to 32. With the increase in δu_x, the length of the membrane along ξ-direction continues to increase as indicated by σ_ξ in Fig. 27. As for σ_η, in contrast to Fig. 22, for nodes 9–20 there is almost no change in σ_η as shown in Fig. 28. This means that there is no reduction in membrane length along η-direction for these nodes. In addition, Fig. 29 shows a decrease in wrinkle amplitude for the same nodes. However, along η-direction, there is an increase in wrinkle number, as shown in Fig. 31. By increasing the wrinkle number, the stress in the membrane is released and the reduction in length along the η-direction is avoided. This increase in wrinkle number is represented by collapsed sections.

From the presented behavior, it can be concluded that the generation of

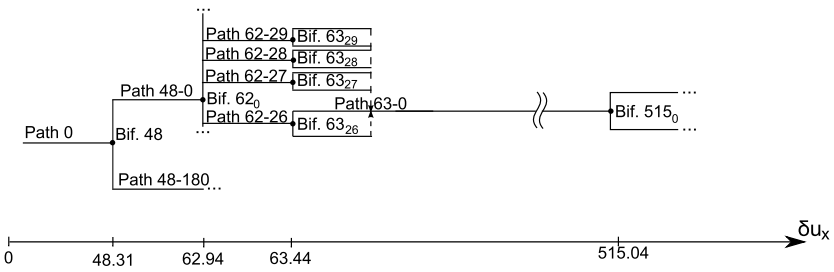

Figure 5: 1:1 cyclic membrane schematic bifurcation diagram

collapsed sections is caused by fixed boundaries. These boundaries generate a stress state of tension and compression and constrain the wrinkle amplitude. For a typical wrinkle, the increasing shear results in an amplitude and frequency increase. Because the fixed boundaries limit the amplitude, the frequency increase is used to relieve the stress in the membrane. The outcome is the generation of collapsed sections.

5.5. Effects of geometry

The above results for the cyclic membrane are based on the 3:1 aspect ratio for the membrane geometry. To observe the effects of different geometry, a membrane with an aspect ratio 1:1 is modeled. The remaining membrane properties are the same as the 3:1 model.

The schematic bifurcation diagram for the 1:1 membrane is in Fig. 5. When compared to the 3:1 bifurcation diagram in Fig. 3, the structure is similar. The difference between the membranes occurs in the δu_x value of bifurcation points after the first bifurcation point. The first bifurcation point is at almost the same value of δu_x because the shell section and material properties for both membranes are the same.

In the 1:1 membrane, the first bifurcation, Bif. 48, generates 10 wrinkles. The second bifurcation, Bif. 62, introduces amplitude variation near the fixed boundaries similarly to the 3:1 membrane. The third bifurcation, Bif. 63, splits one wrinkle and generates 2 new wrinkles resulting in a 12 wrinkle pattern. Path 63-0 maintains the same behavior as Path 69-0 in the 3:1 membrane where collapsed sections are generated. At the fourth bifurcation, a collapsed section reaches a critical size and splits an existing wrinkle and a 14 wrinkle pattern is generated. The wrinkle generation process is the same as can be seen in Fig. 35. In comparison, qualitative behavior is the same for both membranes. The wrinkle generation mechanism following the formation of collapsed sections is also the same. The geometry change causes only a quantitative change in behavior.

Both membranes have a finite length and, as a result, an integer number of wrinkles will always form due to cyclic boundary conditions. In an infinite length membrane, the wrinkle wavelength is determined by the membrane section and

material properties and loads. In a fixed length membrane with cyclic boundary conditions, the wrinkle wave length will round up/down to a value that results in an integer value of wrinkles. The effect of wrinkle wavelength is membrane stability. As can be observed by the results, the more wrinkles are present, the smaller the wrinkle wavelength and a larger value of δu_x needed for a bifurcation point. Therefore, the difference in wrinkle wavelength between the 3:1 and 1:1 membranes can explain the variations in δu_x values of bifurcation points.

6. Conclusion

In this study, the equilibrium path tracking method with the finite element method is used to obtain the wrinkling behavior of rectangular membranes undergoing shear displacement. Initially, a membrane with free boundaries and aspect ratio of 3:1 is analyzed. For this membrane model, by increasing the shear displacement, the entire membrane becomes wrinkled. However, the presence of free boundaries results in an uneven shape and distribution of the wrinkles. By further increase in shear, small wrinkles referred to as collapsed sections are generated on existing wrinkles near fixed boundaries. These sections increase in size and generate new wrinkles. However, the universality of this wrinkle generation behavior may be affected by free boundaries. Therefore, the effect of free boundaries is removed by replacing the free boundaries with cyclic boundaries. By removing the free boundaries and observing the generation of collapsed sections, it is concluded that the cause of collapsed sections are the fixed boundaries. Because fixed boundaries constrain the amplitude of a wrinkle, the additional deformation energy form increasing shear results in an increased wrinkle frequency near the boundary. This increased frequency is represented by collapsed sections. Because fixed boundaries are common in membrane structures, understanding how these boundaries generate new wrinkles is useful in predicting the structure behavior.

7. Vitae

Kei Senda

Kei Senda received the Ph. D. in engineering in 1993 from Osaka Prefecture University. From 1988 to 2008, he worked for Osaka Prefecture University and Kanazawa University. From 2008, has been a professor of Department of Aeronautics and Astronautics, Graduate School of Engineering, Kyoto University. His research activities have included more than 100 papers on the dynamics and control of aerospace systems, the intelligence and autonomy for mechanical systems, and the motion intelligence of animals. He received the Best Presented Paper Award of the AIAA Guidance, Navigation, and Control Conference in 1992, etc.

Mario Petrovic

Mario Petrovic, obtained a bachelor degree in 2008 at the University of Zagreb, Faculty of mechanical engineering and naval architecture, on the topic of numerical simulation of rigid body mechanisms. In 2010, graduated from the University with a master degree on the topic of numerical simulation of dynamic and fatigue in wind turbines. Current position is a doctor course student at Kyoto University, Graduate school of engineering. Here, he conducts research into inflatable structures, where the focus is on the generation of wrinkles in a membrane in an attempt to predict membrane behavior.

Kei Nakanishi

Kei Nakanishi obtained both Bachelor degree in 2010 and Master degree in 2012 from Kyoto University. Their topic is numerical analysis of sheared rectangular membrane in inflatable space structures.

References

[1] A.B. Chmielewsk, Overview of Gossamer Structures in: C.H.M. Jenkins (Eds.), Gossamer Spacecraft: Membrane and Inflatable Structures Technology for Space Applications, AIAA, Reston, VA, 2001, pp.1-20.

[2] K. Senda, T. Oda, S. Ota, Y. Igarashi, A. Watanabe, T. Hori, H. Ito, H. Tsunoda, K. Watanabe, Deploy Experiment of Inflatable Tube using Work Hardening, Proc. AIAA Gossamer Spacecr. Forum, AIAA-2006-1808 (2006) 1-18.

[3] S.P. Timoshenko, J.M. Gere, Theory of Elastic Stability, second ed., Springer, New York, 2010.

[4] Y.W. Wong, S. Pellegrino, Wrinkled Membranes, Part I, J. of Mechanics of Mater. Structures, Vol. 1, No. 1 (2006) 3-25.

[5] Y.W. Wong, S. Pellegrino, Wrinkled Membranes, Part II, J. of Mechanics of Mater. Structures, Vol. 1, No. 1 (2006) 27-61.

[6] Y.W. Wong, S. Pellegrino, Wrinkled Membranes, Part III, J. of Mechanics of Mater. Structures, Vol. 1, No. 1 (2006) 63–95.

[7] R.K. Miller, J.M. Hedgepeth, An Algorithm for Finite Element Analysis of Partly Wrinkled Membranes, AIAA J., Vol. 20, No. 12 (1982) 1761-1763.

[8] R.K. Miller, J.M. Hedgepeth, V.I. Weingarten, P. Das, S. Kahyai, Finite Element Analysis of Partly Wrinkled Membranes, Computers & Structures, Vol. 20, Nos. 1-3 (1985) 631-639.

[9] Y. Miyazaki, Wrinkle/Slack Model and Finite Element Dynamics of Membrane, International J. for Numerical Methods in Engineering, Vol. 66, No. 7 (2006) 1179-1209.

[10] Z.P. Bazant, L. Cedelon, Stability of Structures, Oxford University Press, New York, 1991.

[11] C.G. Wang, X.W. Du, H.F. Tan, X.D. He, A New Computational Method for Wrinkling Analysis of Gossamer Space Structures, International J. of Solids and Structures, Vol. 46, No. 6 (2009) 1516-1526

[12] A. Tessler, D.W. Sleight, J.T. Wang, Effective Modeling and Nonlinear Shell Analysis of Thin Membranes Exhibiting Structural Wrinkling, J. of Spacecr. Rockets, Vol. 42, No. 2 (2005) 287-298.

[13] P. Wiggers, W. Wanger, C. Miehe, A quadratically convergent procedure for the calculation of stability points in finite element analysis, Computer Methods in Appl. Mechanics and Engineering, Vol. 70, No. 3 (1988) 329-347.

[14] J. Leifer, D.C. Jones, A.M. Cook, Gravity-Induced Wrinkling in Subscale, Singly Curved Parabolic Gossamer Membrane, J. of Spacecr. Rockets, Vol. 47, No. 1 (2010) 214-219.

[15] K. Woo, C.H. Jenkins, Effect of Crease Orientation on Wrinkle-Crease Interaction for Thin Membranes, J. of Spacecr. Rockets, Vol. 50, No. 5 (2013) 1024-1034.

[16] A. Tessler, D.W. Sleight, Geometrically Nonlinear Shell Analysis of Wrinkled Thin-Film Membranes with Stress Concentrations, J. of Spacecr. Rockets, Vol. 44, No. 3 (2007) 582-588.

[17] S. Inoue,Prediction Methods of Wrinkling in Thin-Membrane, Proc. of International Symposium on Space Technology and Science, Tsukuba, Japan, (2009) 1-7.

[18] A. Endo, Y. Hangai, S. Kawamata, Post-Buckling Analysis of Elastic Shells of Revolution by the Finite Element Method, Rep. of Inst. of Industrial Science, 624.074.4:624.075.4 (1976).

[19] P. Wriggers, W. Wanger, C. Miehe, A Quadratically Convergent Procedure for the Calculation of Stability Points in Finite Element Analysis, Computer Methods in Appl. Mechanics and Engineering, Vol. 70, No. 3 (1988) 329-347.

[20] R. Hoyle, Pattern Formation, Cambridge University Press, New York, 2007.

[21] B.S. Reddy, B. N. Chatterji, An FFT-based technique for translation, rotation, and scale-invariant image registration,' IEEE Transactions on Image Processing 5, Vol. 5, No. 8 (1996) 1266-1271.

[22] K. Senda, K. Nakanishi, K. Takagi, Wrinkle Generation Mechanism without Buckling in Sheared Rectangular Membrane, Proc. AIAA Gossamer Spacecr. Forum, AIAA-2012-1919 (2012).

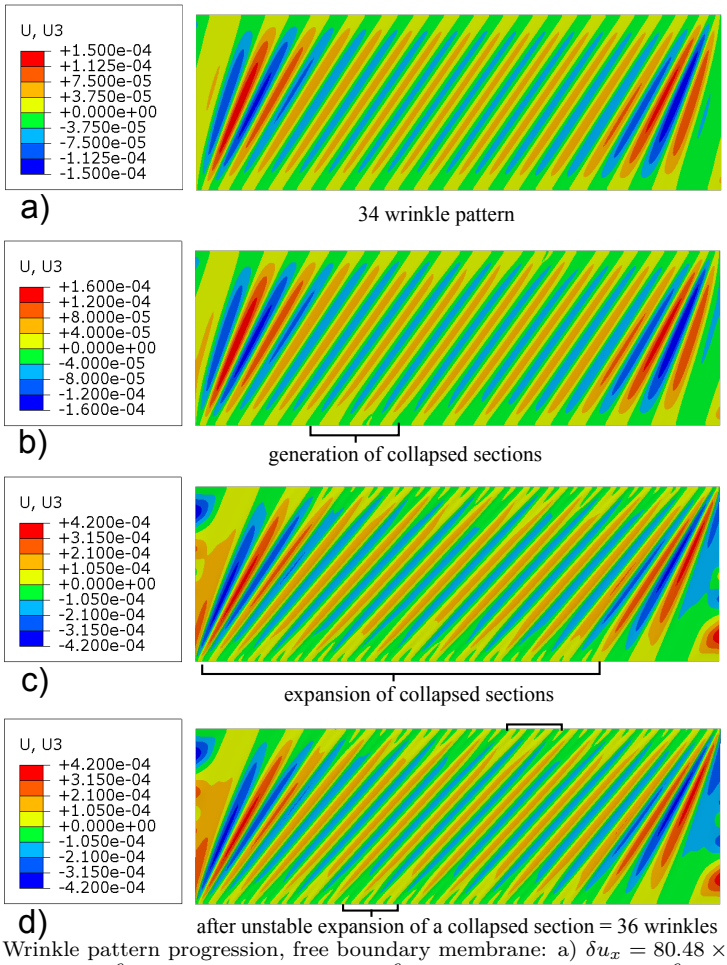

Figure 6: Wrinkle pattern progression, free boundary membrane: a) $\delta u_x = 80.48 \times 10^{-6}$[m]; b) $\delta u_x = 90.00 \times 10^{-6}$[m]; c) $\delta u_x = 440.00 \times 10^{-6}$[m]; d) $\delta u_x = 440.21 \times 10^{-6}$[m].

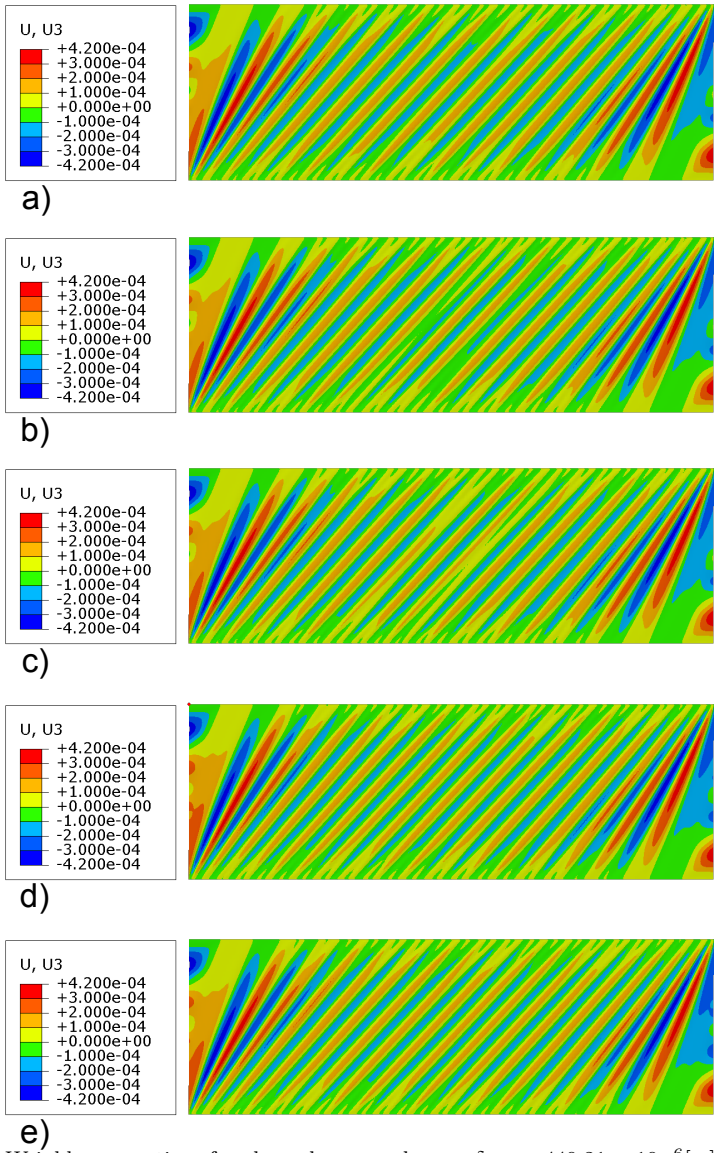

Figure 7: Wrinkle generation, free boundary membrane, $\delta u_x = 440.21 \times 10^{-6}$[m]: a) initial condition, b) convex down wrinkle split, c) convex up wrinkle split, d) final pattern after convex down wrinkle split, e) final pattern after convex up wrinkle split.

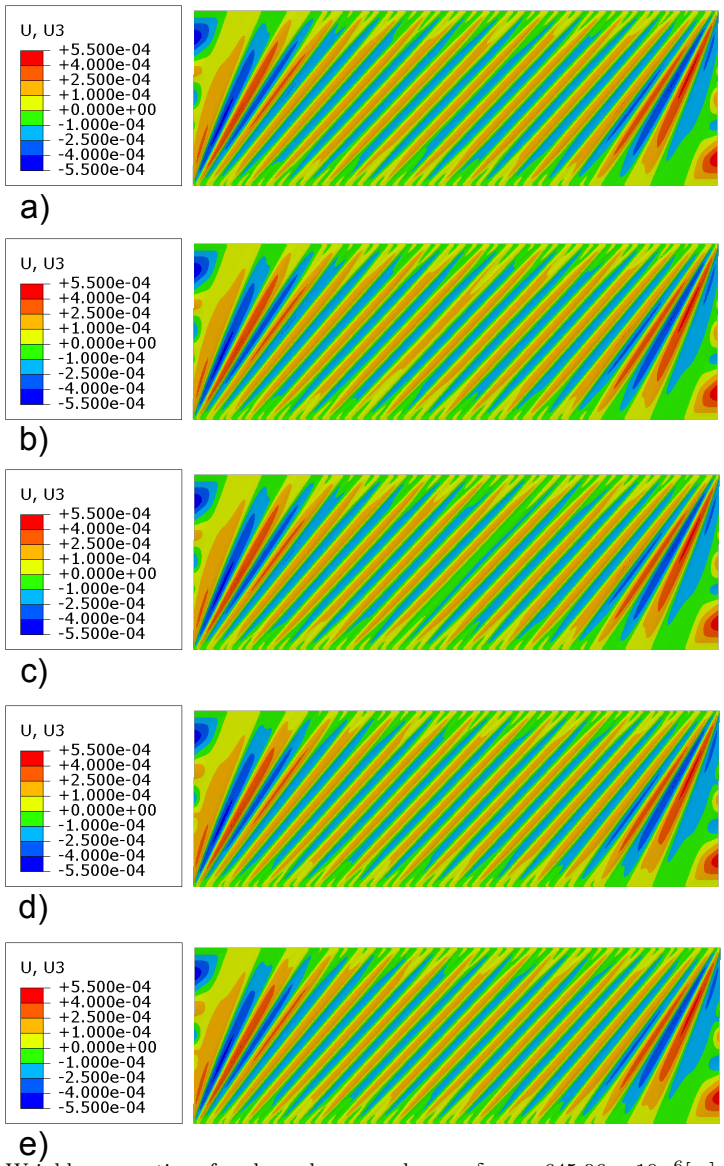

Figure 8: Wrinkle generation, free boundary membrane, $\delta u_x = 645.96 \times 10^{-6}$[m]: a) initial condition, b) convex down wrinkle split, c) convex up wrinkle split, d) final pattern after convex down wrinkle split, e) final pattern after convex up wrinkle split.

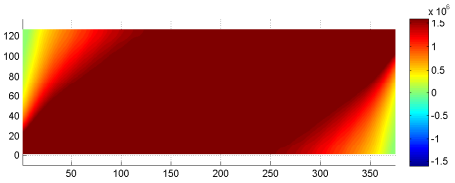

Figure 9: First principal stress, σ_ξ, free boundary membrane.

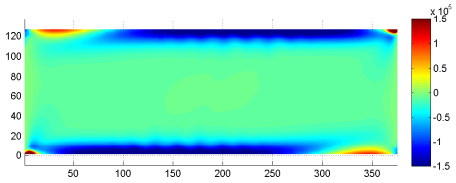

Figure 10: Second principal stress, σ_η, free boundary membrane.

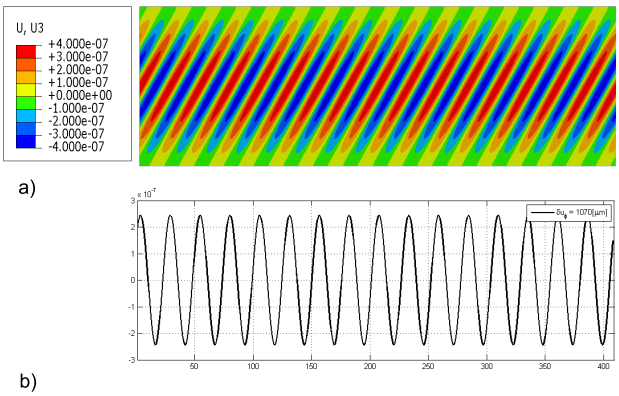

Figure 11: Out-of-plane deformation after Bif. 48, cyclic boundary membrane.

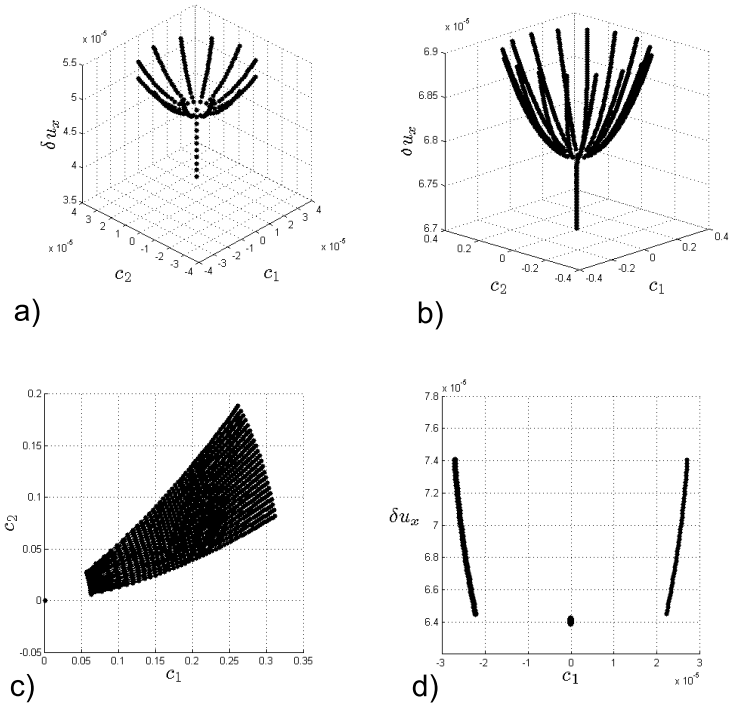

Figure 12: Bifurcation diagrams for cyclic membrane; a) Bif. 48, b) Bif. 67, c) close up after Bif. 67, d) Bif. 69.

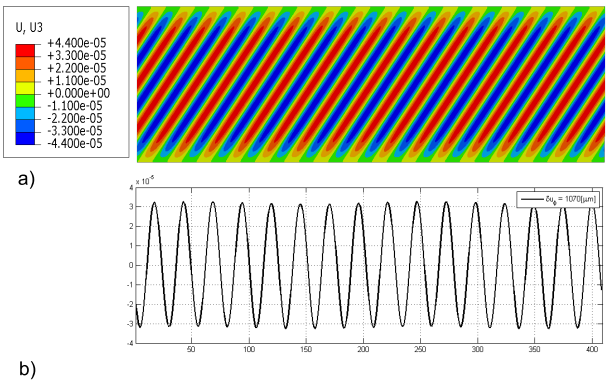

Figure 13: Out-of-plane deformation after Bif. 67, cyclic boundary membrane.

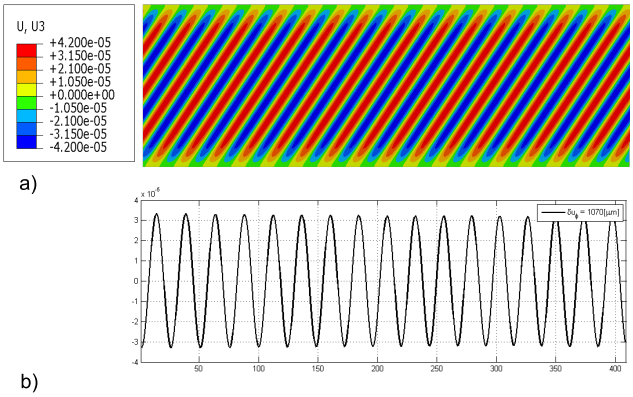

Figure 14: Out-of-plane deformation after Bif. 69, cyclic boundary membrane.

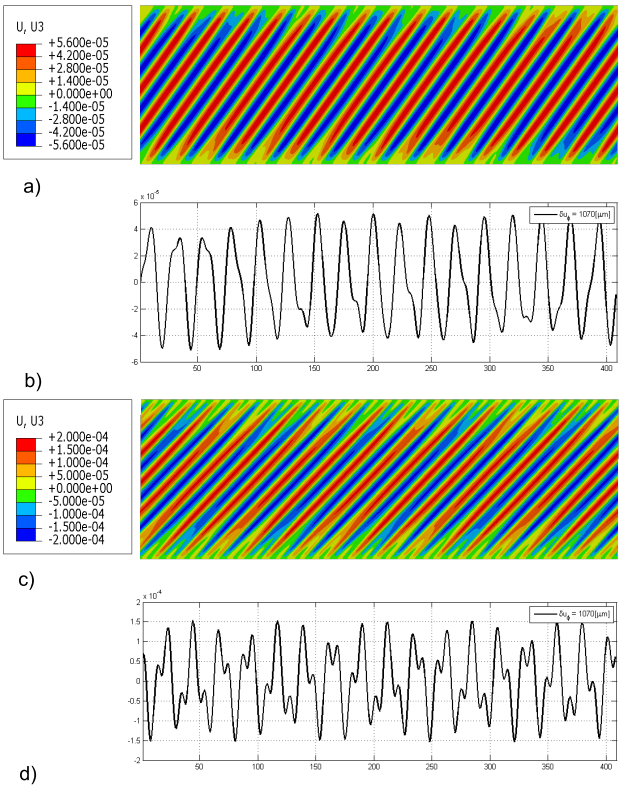

Figure 15: Out-of-plane deformation on Path 69-0, cyclic boundary membrane.

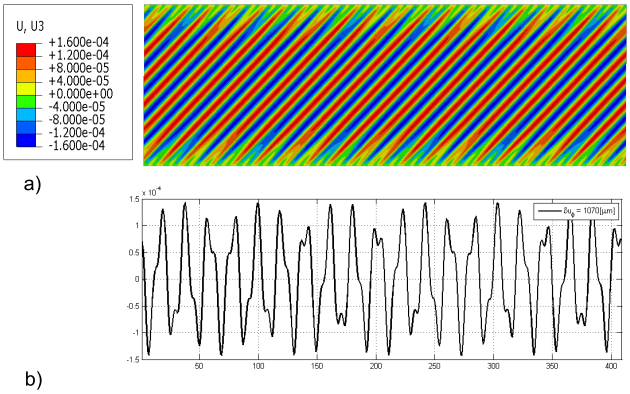

Figure 16: Out-of-plane deformation, Bif. 500, cyclic boundary membrane.

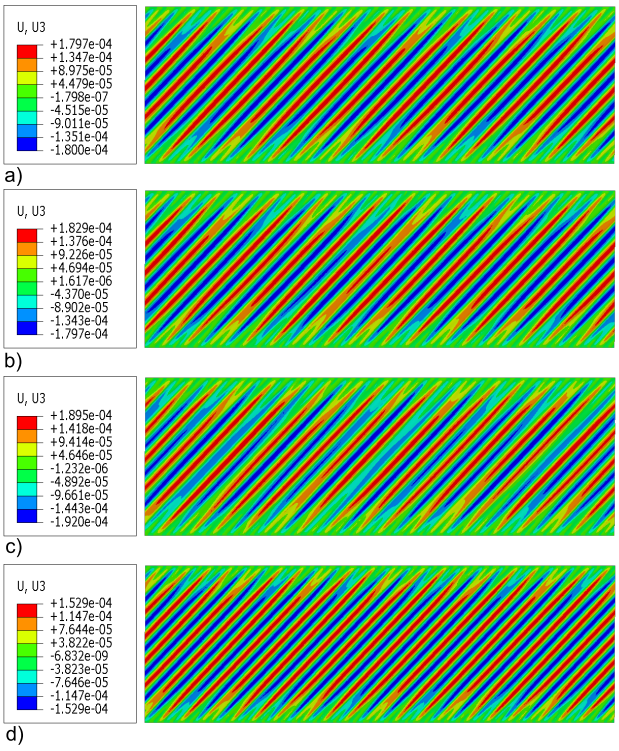

Figure 17: Wrinkle split, Bif. 500, cyclic boundary membrane: a) initial condition, b) start of rapid collapsed section expansion, c) wrinkle splitting, d) final wrinkle pattern.

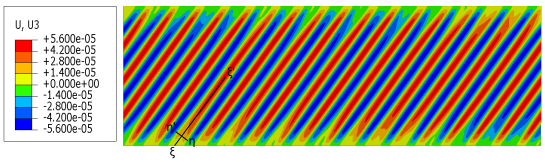

Figure 18: Sections $\xi\xi'$ and $\eta\eta'$ positioning for Path 69.

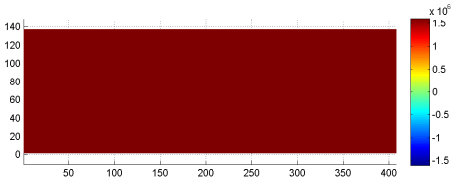

Figure 19: First principal stress, σ_ξ.

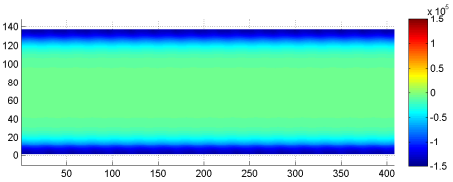

Figure 20: Second principal, σ_η.

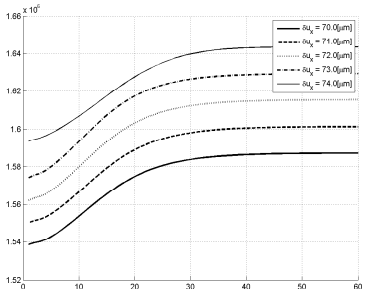

Figure 21: First principal stress, σ_ξ, section $\xi\xi'$.

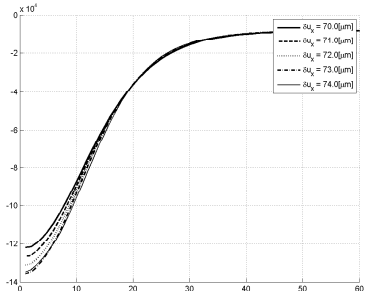

Figure 22: Second principal, σ_η,section $\xi\xi'$.

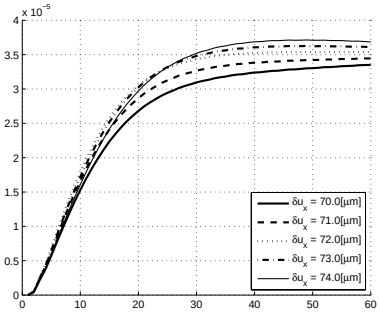

Figure 23: Out-of-plane displacement, u_z, section $\xi\xi'$.

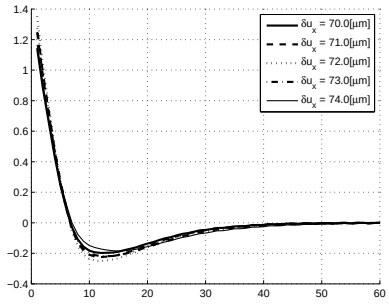

Figure 24: Curvature, κ_η, section $\xi\xi'$.

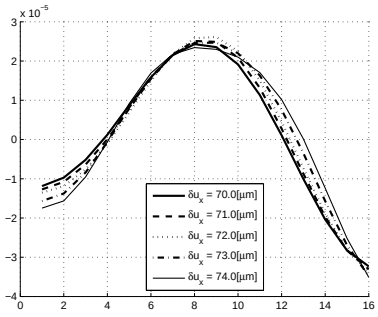

Figure 25: Out-of-plane displacement, u_z, section $\eta\eta'$.

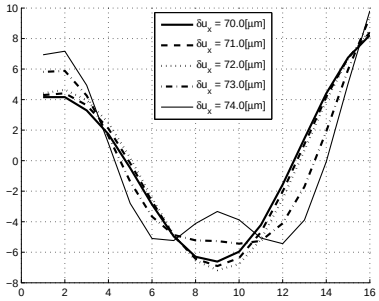

Figure 26: Curvature, κ_ξ, section $\eta\eta'$.

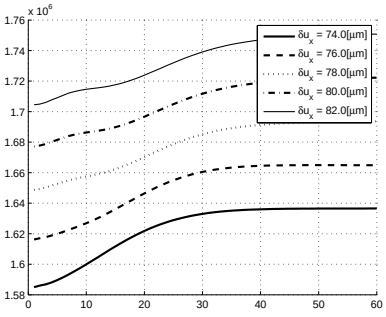

Figure 27: First principal stress, σ_ξ, section $\xi\xi'$.

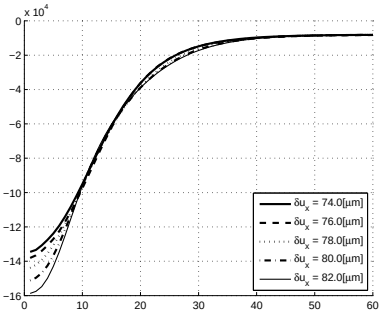

Figure 28: Second principal, σ_η,section $\xi\xi'$.

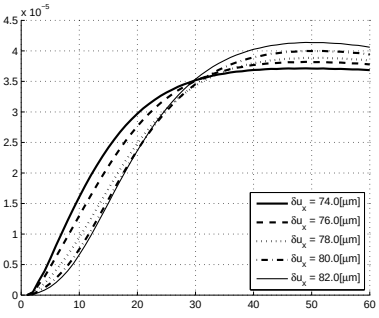

Figure 29: Out-of-plane displacement, u_z, section $\xi\xi'$.

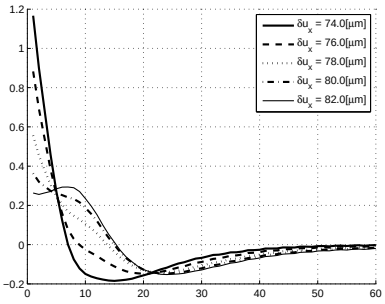

Figure 30: Curvature, κ_η, section $\xi\xi'$.

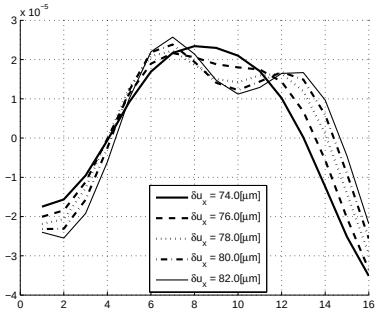

Figure 31: Out-of-plane displacement, u_z, section $\eta\eta'$.

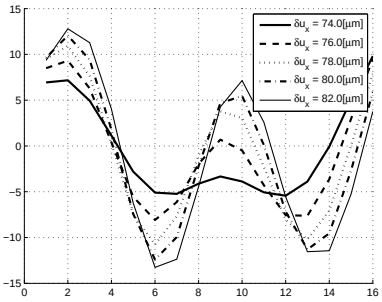

Figure 32: Curvature, κ_ξ, section $\eta\eta'$.

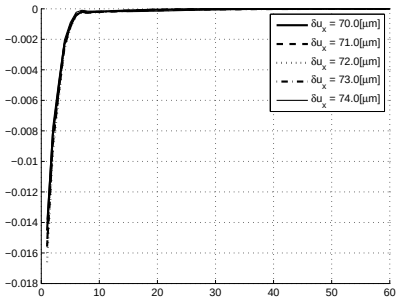

Figure 33: Shell section transversal force, Q_ξ, section $\xi\xi'$.

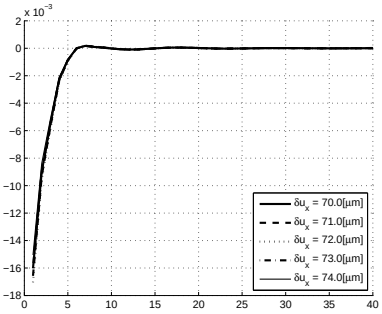

Figure 34: Shell section transversal force, Q_η, section $\eta\eta'$.

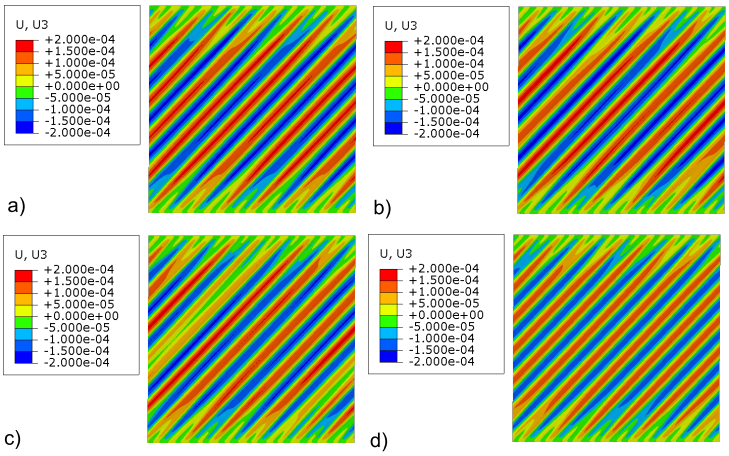

Figure 35: Wrinkle split, Bif. 515, 1:1 cyclic boundary membrane: a) initial condition, b) start of rapid collapsed section expansion, c) wrinkle splitting, d) final wrinkle pattern.

Figure 36: Author: Kei Senda

Figure 37: Author: Mario Petrovic

Figure 38: Author: Kei Nakanishi (placeholder)